ISSN: 3023 -8951

CHAOS AND FRACTALS

VOLUME 2, ISSUE 1, JANUARY 2025

AN INTERDISCIPLINARY JOURNAL OF NONLINEAR SCIENCE

ADBA

https://journals.adbascientific.com/chf

ISSN: 3023-8951

Chaos and Fractals

Volume: 2 – Issue No: 1 (January 2025)

EDITORIAL BOARD

https://journals.adbascientific.com/chf/about/editorialTeam

ISSN: 3023-8951

Chaos and Fractals
Volume: 2 – Issue No: 1 (January 2025)

CONTENTS

1 **Awais Khan, Chunbiao Li, Xin Zhang, Xiaoliang Cen**
A Two-Memristor-based Chaotic System with Symmetric Bifurcation and Multistability **(Research Article)**

8 **Muhammed Furkan Taşdemir, Murat Tuna, Ismail Koyuncu**
FPGA-Based Chaotic Oscillator Designs and Performance Analysis **(Research Article)**

14 **Rolande Tsapla Fotsa, Paloma Kevina Koubeu Papemsi, Gideon Pagnol Ayemtsa Kuete, Justin Roger Mboupda Pone, Serge Raoul Dzonde Naoussi, Foutse Momo, Pierre Ele**
Permanent Magnet Synchronous Motor with Load Torque: Dynamics, Circuitry Execution and Control **(Research Article)**

20 **Berkay Emin, Yusuf Uzunoğlu, Yusuf Alaca**
Investigation of the Impact of Alloying Elements on the Mechanical Properties of Superalloys Using Explainable Artificial Intelligence **(Research Article)**

https://journals.adbascientific.com/chf/issue/view/8

ADBA Chaos and Fractals
Cutting-Edge Scientific Solutions

e-ISSN: 3023-8951
RESEARCH ARTICLE
Vol.2 / No.1 / 2025 / pp.1-7
https://doi.org/10.69882/adba.chf.2025011

A Two-Memristor-based Chaotic System with Symmetric Bifurcation and Multistability

Awais Khan [*,1], **Chunbiao Li** [*,2], **Xin Zhang** [α,3] **and Xiaoliang Cen** [α,4]

*Nanjing University of Information Science & Technology, School of Artificial Intelligence, 210044, Nanjing, People's Republic of China, αNanjing University of Information Science & Technology, School of Electronic and Information Engineering, 210044, Nanjing, People's Republic of China.

ABSTRACT In this work, the study of an innovative chaotic system made from two memristors with symmetric bifurcation and multistability is presented. Within a four-dimensional chaotic framework, the system is architected with two flux-controlled memristors. Computational simulations reveal intricate dynamical phenomena such as symmetric bifurcations, multistability, and very large sensitivity to initial conditions. Using Lyapunov exponents, bifurcation diagrams, and phase portraits we investigate the system's ability to produce chaotic attractors of pronounced multistability. Pinched hysteresis loop and system offset investigation at different frequencies are investigated for possible applications in neuromorphic computing, random number generation, and secure communication protocols. We further advance our understanding of the complex dynamical properties of memristive chaotic systems. A representative analog circuit corroborates their numerical findings.

KEYWORDS
Multistability
Analog circuit
Chaotic systems
Bifurcation

INTRODUCTION

The exploitation of chaotic systems has been a main field of academic inquiry due to the many applications in secure communication, stochastic number generation, image encryption (Umar *et al.* 2024), and neuromorphic computing (Masominia 2024). In particular, memristor-based chaotic circuits (Kumari and Yadav 2023) stand out from the myriad approaches due to exceptional nonlinear properties and memristor-based memory-dependent resistance (Li *et al.* 2023). The memristor was shown to be a revolutionary element designed for nonlinear systems (Penington 2022). It is specifically well suited to chaos-oriented applications due to its ability to replicate biological synapses and exhibit intricate dynamics (Lin *et al.* 2023). Scholarly interest in memristor-based chaotic systems has been piqued for their potential applications in secure communication, random number generation, and adaptive circuits (Wei *et al.* 2024). Despite that, the existing literature is mainly about standalone memristor architectures and fails to explore the full potential of the entire set of memristors. However, two memristor-based systems remain poorly explored, in particular for their ability to increase chaos generation, symmetric bifurcation (Li *et al.* 2021), and multistability (Fang *et al.* 2022). Moreover, balanced and predictable dynamics are facilitated by symmetric bifurcation, whereas diverse and reconfigurable behaviors are supported by multistability.

The fundamental nonlinearity of the memristor brings forth a prominent characteristic of its volt-ampere characteristic curve for the memristor, which is represented by a narrowing hysteresis loop (Luo *et al.* 2023). Memristor nonlinearity embedded in the memristor fosters the development of chaotic systems exhibiting rich dynamic behaviors, such as chaos, oscillations burst multistability states, etc. (Yang *et al.* 2024). In this context, the exploration of memristive chaotic systems warrants a closer look in the field of nonlinear sciences because of the rich dynamic behaviors induced by chaotic systems realized with memristors. A considerable amount of academic research has been of interest in recent years (Lai *et al.* 2023). The controller was incorporated into the foundational memristor chaotic system to formulate a chaotic system and assess its multistability. A memristive chaotic system with remarkable multistability was introduced in the phenomenon and comprehensive studies (Bao *et al.* 2022b).

A foundational chaotic oscillating circuit incorporating a memristor that is characterized by minimal nonlinearity and bifurcation diagrams is used to explain the appearance of previously unanticipated dynamical features in the circuit (Marszalek 2022). The multiple attractors within a memristive diode bridge jerk circuit were revealed and the trajectory toward a chaotic state was investigated (Fossi *et al.* 2023). Additionally, a memristor is added to the jerk circuit and found to exhibit various dynamic attributes including multistability and monotonic behavior (Kamdem Tchiedjo *et al.* 2022).

However, a preponderance of modern academic inquiries concerns individual memristor configurations, disregarding the potential of chaotic systems consisting of dual memristors (Wang *et al.* 2024; Bao *et al.* 2022a; Guo *et al.* 2021). These rationales lead to this

Manuscript received: 21 January 2025,
Revised: 28 January 2025,
Accepted: 28 January 2025.

[1]awaiskhan3017@gmail.com (**Corresponding author**)
[2]chunbiaolee@nuist.edu.cn
[3]xinzhang96@nuist.edu.cn
[4]xiaoliangcen@nuist.edu.cn

investigation that seeks to address the gap by leveraging the interactions between a pair of memristors to enhance chaos generation, symmetric bifurcation (Guo *et al.* 2021), and multistability (Boya *et al.* 2022). In addition, further characteristics are elucidated as follows:

1. Investigate the profound multistability exhibited by a chaotic system comprising two memristors, which is contingent upon the initial conditions, through the application of a dimensionality reduction model. This methodology enables accurate forecasting examination and regulation of multistability via recognized quantitative methodologies.

2. Examine the essential dynamics, encompassing bifurcation and chaotic phenomena through the manipulation of system parameters and the subsequent observation of resultant behaviors.

3. Devise and execute an analog circuit to substantiate the theoretical conclusions, guaranteeing that the computational simulations are consistent with the empirical data.

By using the dynamics of the dimensionality reduction model to recreate the initial parameters-dependent extreme multistability in the two-memristor chaotic system, one may precisely forecast, analyze, and control extreme multistability using traditional quantitative methods.

In this article, we lay out the methodical organization of the manuscript. We focus on the evaluation of equilibrium points, Lyapunov exponents, and Kaplan-Yorke dimensions in Section 2, which describes the internal dynamics of the suggested chaotic system with two memristors. Section 3 offers an extensive exposition of the essential dynamics, encompassing chaotic attractors, bifurcation diagrams, and frequency-domain responses. Section 4 investigates the adjustable chaotic dynamics manifested by the system. Within Section 5, the occurrence of multiple attractors is scrutinized, with a specific focus on the principles of multistability and symmetric bifurcations as modulated by varied initial conditions. Section 6 articulates the conceptualization and implementation of a demonstrative analog circuit employing components such as operational amplifiers and capacitors, intended to corroborate the theoretical insights through empirical validation. The concluding section integrates the exhaustive findings and implications of the research endeavor.

MODEL AND ITS FUNDAMENTAL DYNAMICS

Chaotic Analysis of a Novel System

In this segment, we presented a novel four-dimensional framework characterized by:

$$\begin{cases} \dot{x} = -x(0.2y^2 - 0.5) - z|aw| - b \\ \dot{y} = x - 2y + 2x^2y \\ \dot{z} = x \\ \dot{w} = w - w|w| - z \end{cases} \tag{1}$$

The variables x, y, z, and w are considered independent, while the parameters a and b are positive real numbers. Altering the parameters, a and b can induce system (1) to demonstrate chaotic, periodic, or quasi-periodic behavior.

Evaluation of Equilibria

The equilibria represented by equation 1 can be determined through:

$$\begin{cases} -x(0.2y^2 - 0.5) - z|aw| - b = 0 \\ x - 2y + 2x^2y = 0 \\ x = 0 \\ w - w|w| - z = 0 \end{cases} \tag{2}$$

Equation 2 can be analyzed through analytical techniques, considering its unique equilibrium point, which is represented as S_0 $(0, 0, -0.3854, 1.2971)$. The Jacobian matrix can be formulated by linearizing Equation 1 around the zero-equilibrium point S_0:

$$J = \begin{bmatrix} 0.5 & 0 & -2.5942 & 0.7708 \\ 1 & -2 & 0 & 0 \\ 0 & 0 & 0 & 0 \\ 0 & 0 & -1 & -1.5942 \end{bmatrix} \tag{3}$$

We get the characteristic equation at S_0:

$$\det(\lambda I - J) = (a_4\lambda^4 + a_3\lambda^3 + a_2\lambda^2 + a_1\lambda^1) = 0 \tag{4}$$

Given the presence of positive Lyapunov exponents (λ_3 and λ_4), it can be inferred that the system may exhibit chaotic dynamics or unstable trajectories along certain axes. Conversely, the negative exponent (λ_1 and λ_2) implies the existence of stability along a specific direction. The system cannot be characterized as exhibiting solely stable behavior due to the presence of a positive exponent. By setting the parameters to $a = 2$ and $b = 1$, the eigenvalues relevant to the state S_0 are determined as:

$$\begin{cases} \lambda_1 = 0.3103 + 1.6628i, \\ \lambda_2 = 0.3103 - 1.6628i, \\ \lambda_3 = -1.7148, \\ \lambda_4 = -2. \end{cases} \tag{5}$$

Dimension of Kaplan-Yorke and Lyapunov Exponents

Equation 1 can be resolved utilizing the `ode45` algorithm within the MATLAB computational environment, with parameters $a = 2$ and $b = 1$ being held constant. The discretization step size is established at 0.005, which is derived from a comprehensive analysis involving one million computations. Later, with the original setup $[0.1, 0, 0, 0]$, the evaluated Lyapunov exponents were $\lambda_1 = 0.3103$, $\lambda_2 = 0.3103$, $\lambda_3 = -1.7148$, $\lambda_4 = -2$. The Kaplan-Yorke dimension of system (1) is assessed as:

$$D_{KY} = 3 + \frac{\sum_{i=1}^{3} \lambda_i}{|\lambda_4|} \tag{6}$$

$$D_{KY} = 3 + \frac{0.3103 + 0.3103 - 1.7148}{-2} = 3.5471 \tag{7}$$

The presence of an anomalous attractor is assured by the fractional quantity referred to as the Kaplan-Yorke dimension (Silva-Juárez *et al.* 2021). In Figure 1, the chaotic attractors are illustrated, while in Figure 2 it depicts the chaotic waveform, and Figure 3 represents the frequency of the chaotic signals. The signal w exhibits a reduced frequency relative to the chaotic signals.

ANALYSIS OF CHAOTIC ATTRACTORS

The chaotic attractors depicted in Figure 1 exemplify the dynamic behavior exhibited by the chaotic system based on two memristors, when the parameters $a = 2$ and $b = 1$, alongside the initial conditions $[0.1, 0, 0, 0]$. The attractors reveal intricate, non-periodic trajectories across various planes, thereby validating the chaotic characteristics of the system. Noteworthy attributes include symmetric, layered loops situated in the y-z plane, elongated and overlapping loops found in the x-z plane, and stretched intersecting loops present in the x-w plane, highlighting substantial nonlinear interactions and symmetrical bifurcation. The findings illustrate the system's ability to generate a spectrum of tunable chaotic behaviors, signifying its prospective applications in secure communication and adaptive circuitry.

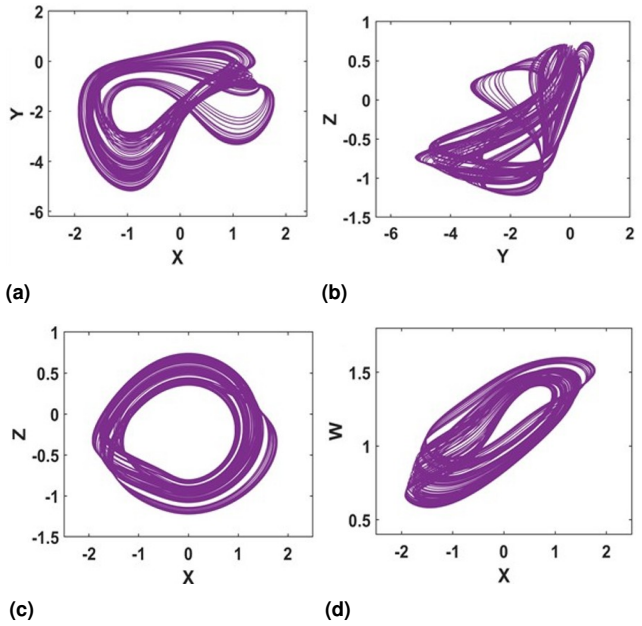

Figure 1 Chaotic attractors in different planes of equation 1 with $a = 2$ and $b = 1$ under the initial conditions $[0.1, 0, 0, 0]$: (a) x-y, (b) x-z, (c) y-z, (d) x-w.

Figure 2 delineates the erratic waveforms exhibited by the two-memristor-based chaotic system when parameters $a = 2$ and $b = 1$ are applied, under the initial conditions of $[0.1, 0, 0, 0]$. The variable outputs $x(t)$, $y(t)$, $z(t)$, and $w(t)$ exhibit irregular oscillatory patterns, which validates the chaotic features embedded within the system. Every variable displays particular amplitudes and frequencies: $x(t)$ and $w(t)$ vary within the confines of $[-2, 2]$, $y(t)$ extends from $[-6, 2]$, and $z(t)$ is bounded to $[-2, 1]$. These findings underscore the system's capacity to generate intricate, non-periodic signals that are suitable for chaos-based applications.

BIFURCATION DIAGRAMS AND LYAPUNOV EXPONENT SPECTRA

Figure 4a and 4b serve to elucidate the dynamical characteristics of the system by employing Lyapunov exponents (LEs) and bifurcation diagrams corresponding to parameter variations in a and b, respectively, under the initial conditions $[0.1, 0, 0, 0]$. When $a = 2$, the Lyapunov exponents reveal zones of chaotic dynamics, as evidenced by the positive values of the primary exponent (LE1), thereby affirming the system's pronounced sensitivity to initial

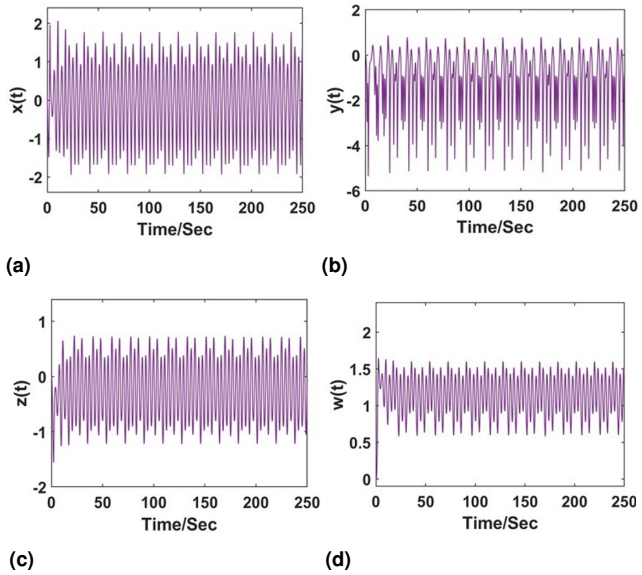

Figure 2 Chaotic Waveform of equation 1 with $a = 2$ and $b = 1$ under the initial condition $[0.1, 0, 0, 0]$: (a) waveform $x(t)$, (b) waveform $y(t)$, (c) waveform $z(t)$, (d) waveform $w(t)$.

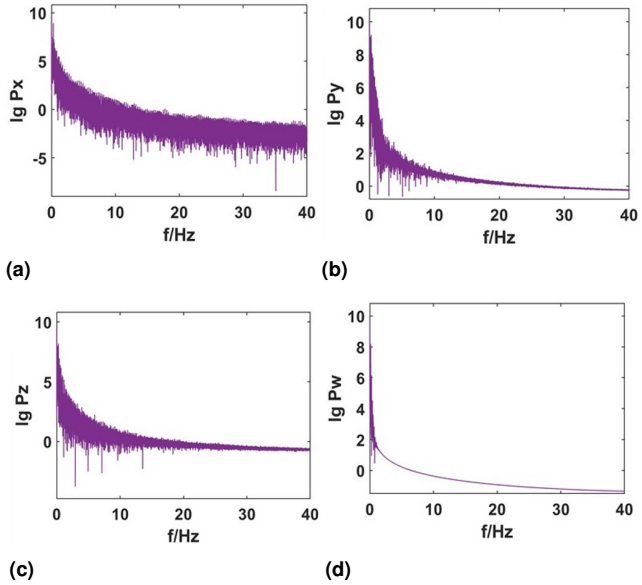

Figure 3 Frequency spectra of equation 1 with $a = 2$ and $b = 1$ under the initial conditions $[0.1, 0, 0, 0]$.

conditions. The bifurcation diagram delineates the emergence of both periodic and chaotic attractors as the parameter varies, exhibiting intricate branching patterns that encapsulate the system's dynamics. For parameter a set to 2, the Lyapunov exponents corresponding to the system (1) are represented in Fig. 4(a) as $(0.0037, -0.0469, -0.0526)$. The bifurcation diagrams of the system (1) across maximum value $[1, 2]$ at each iteration are presented in Figure 4b.

In a similar vein, when $b = 1$, the Lyapunov exponents and bifurcation diagrams unveil a comparable dynamic interplay between periodic and chaotic regimes. The positive Lyapunov exponents (LE1) corroborate the existence of chaotic domains, while the bifurcation diagram graphically represents the presence of mul-

tiple coexisting attractors and transitions between periodic and chaotic dynamics. The findings underscore the intricate dynamical behavior of the system and its adaptable characteristics through parameter variations, rendering it suitable for applications that require controllable chaos (Chaintron and Diez 2021). For a value of parameter $b = 1$, the Lyapunov exponents associated with the system (1) are $(0.0956, 0, -0.3507)$, represented in Fig. 6(a). The bifurcation diagrams of the system (1) across maximum value $[-5, 5]$ at each iteration are presented in Fig. 6b.

The preceding analysis leads to the understanding that the recommended nonlinear model can yield multiple kinds of oscillations within the nonlinear context like behaviors such as quasi-periodic, chaotic or periodic (Kuznetsov *et al.* 2023a). This significantly augmented the complexity associated with equation 1.

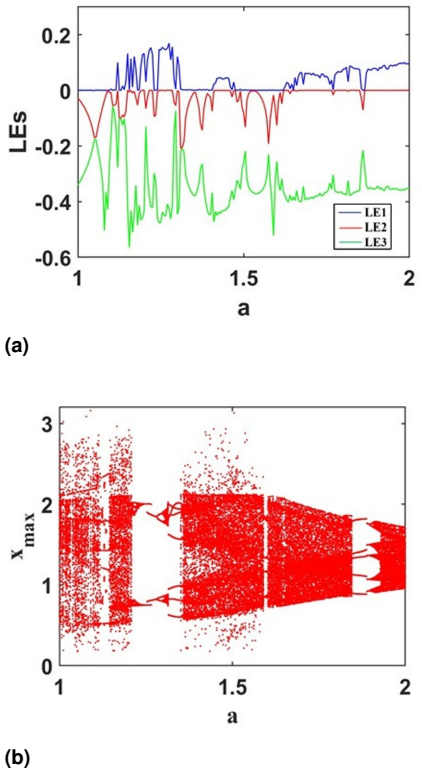

Figure 4 Dynamical behavior of equation 1 with $b = 1$ under initial conditions $[0.1, 0, 0, 0]$: (a) Lyapunov exponents, (b) bifurcation diagram.

Figure **??** illustrates the intricate dynamics of a nonlinear system as it responds to fluctuations in parameter values, specifically with b held constant at 1, while employing the initial condition of $[0.1, 0, 0, 0]$. The phase portraits delineate various modes of motion, which evolve as the parameter a is incremented. At lower values, specifically $a = 0.1$, the system demonstrates periodic behavior, typified by stable and recurrent orbits. As parameter a is increased to values such as $a = 0.8$ or $a = 2.4$, the system transitions into a regime of quasi-periodic motion, wherein the trajectories remain confined yet do not exhibit repetition. At an intermediate value of a, specifically $a = 1.6$, the system reveals chaotic dynamics, characterized by trajectories that possess multiple positive Lyapunov exponents, indicating a heightened level of complexity. For elevated values of a such as $a = 5.8$, the system manifests chaotic behavior, exhibiting sensitive dependence on initial conditions and a complex structural configuration. The parameter a governs the system's rich and multifaceted dynamics which are highlighted by these transitions among periodic, quasi-periodic, and chaotic regimes.

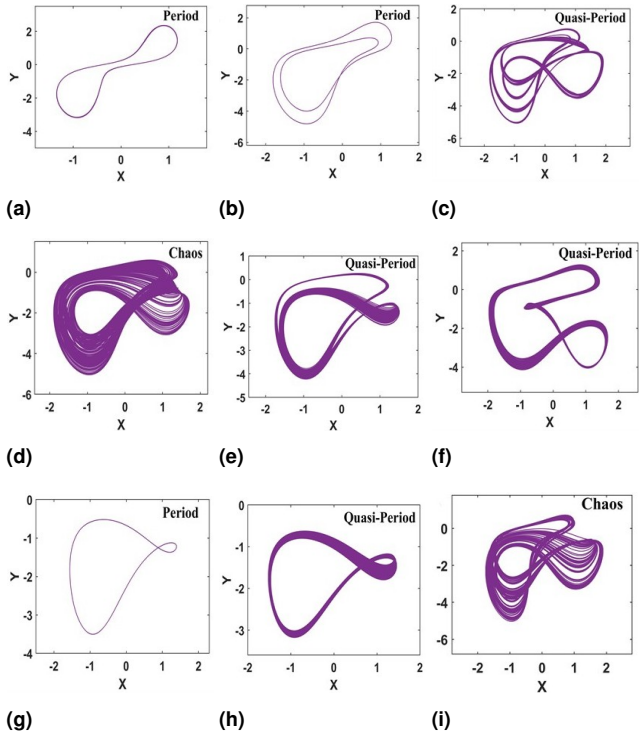

Figure 5 Typical phase portraits of equation 1 with fixed $b = 1$ under the initial condition $[0.1, 0, 0, 0]$: (a) $a = 0.1$, (b) $a = 0.8$, (c) $a = 1.6$, (d) $a = 2.1$, (e) $a = 2.4$, (f) $a = 3$, (g) $a = 4$, (h) $a = 5.5$, (i) $a = 5.8$.

Figure 7 delineates the dynamic characteristics of the nonlinear system under the constraint of a fixed parameter $a = 2$ while systematically varying the parameter b, commencing from the initial condition $[0.1, 0, 0, 0]$. When $b = 1$, the system manifests chaotic behavior, exhibiting trajectories of considerable complexity. As b is incremented to $b = 0.8$, the system transitions to quasi-periodic motion, where the trajectories remain confined yet do not exhibit repetition. At $b = 1.6$, chaotic dynamics are discerned, revealing a pronounced sensitivity to initial conditions. Ultimately, for $b = 2.1$, the system evolves into a periodic state, characterized by stable and repetitive orbits. This illustrates the system's capacity to transition among various dynamical states in response to alterations in the parameter b.

With beginning circumstances set to initial condition IC1 = $[0.1, 0, 0, 0]$ and IC2 = $[-0.1, 0, 0, 0]$, our system is shown in Figure 8 operating under the control of parameters $a = 2$ and $b = 1$. One can see the $x - w$ phase plane in Figure 8a, highlighting two unique attractors (represented in blue and red) that reflect the occurrence of periodic or quasi-periodic activity. Figure 8b outlines the temporal waveform $w(t)$, which elucidates two separate oscillatory patterns corresponding to the recognized attractors. The system exhibits intricate oscillatory behavior marked by variances in both amplitude and frequency.

MULTISTABILITY ANALYSIS

Multistability denotes the simultaneous existence of multiple trajectories under identical system parameters, characterized by distinct

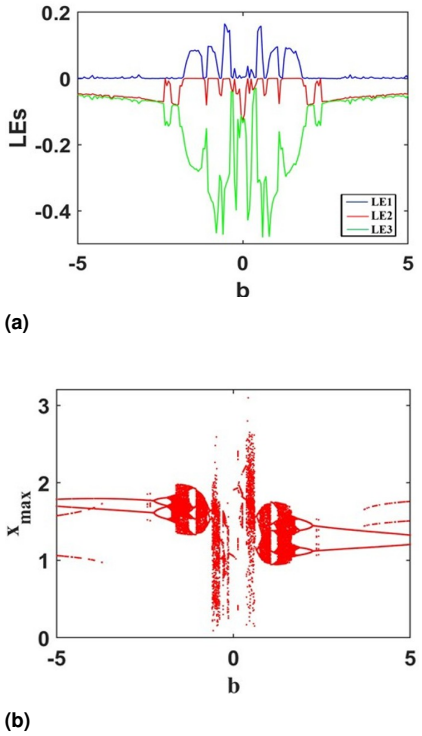

Figure 6 Dynamical behavior of equation 1 with $a = 2$ under initial conditions $[0.1, 0, 0, 0]$: (a) Lyapunov exponents of parameter b, (b) bifurcation diagram of variable x.

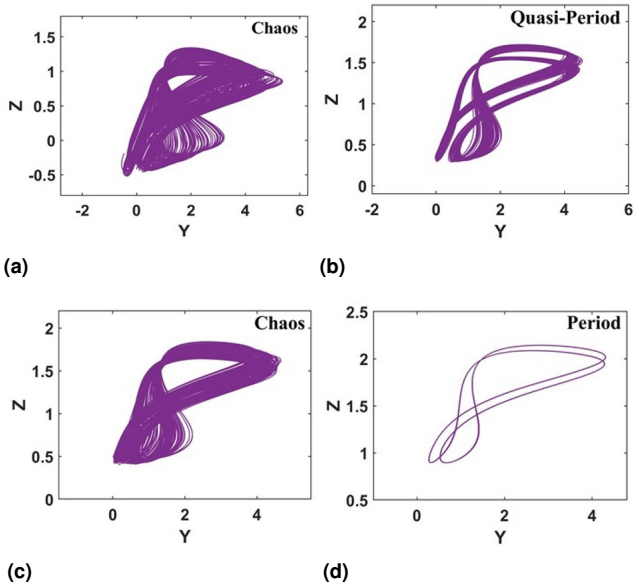

Figure 7 Typical phase portraits of equation 1 with fixed $a = 2$ under the initial condition $[0.1, 0, 0, 0]$: (a) $b = 1.5$, (b) $b = 3.6$, (c) $b = 4.1$, (d) $b = 6$.

initial conditions. Systems exhibiting multistability characteristics within chaotic dynamics are particularly advantageous for a plethora of applications in the engineering domain. This section employs Lyapunov exponents and symmetric attractors to examine the multistability intrinsic to the system under investigation. Figure 9 delineates the dynamic properties of the system for pa-

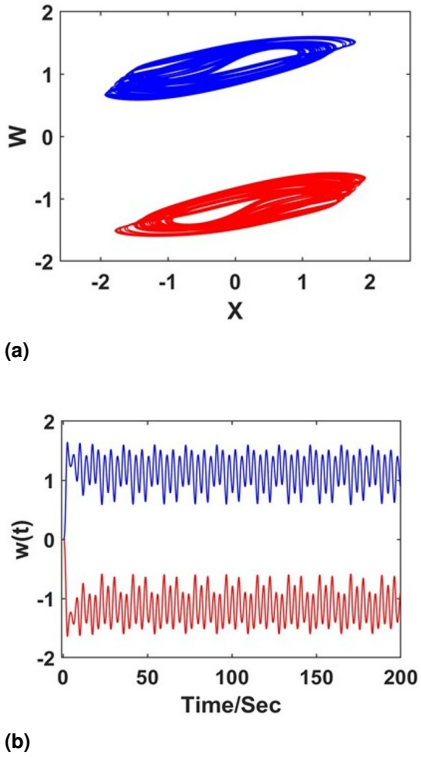

Figure 8 Coexisting symmetric chaotic attractors of equation with $a = 2$ under the initial condition IC1 = $[0.1, 0, 0, 0]$ (blue), IC2 = $[-0.1, 0, 0, 0]$ (red): (a) $x - w$ plane, (b) waveform $w(t)$.

rameter values $a = 2$ and $b = 1$, in conjunction with varying initial conditions. In Figure 9a, the observation reveals that the mean values of the system variables (x, y, z, and w) stay unchanged as $x(0)$ transitions from -5 to 5, demonstrating the equilibrium state of the system throughout this period. Figure 9b presents the Lyapunov exponents (LEs), where one exponent is marginally positive, thereby affirming the existence of chaotic dynamics, while the other exponents are negative, indicating bounded and stable trajectories within the chaotic framework.

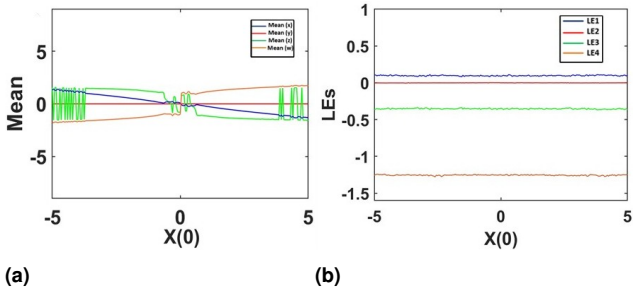

Figure 9 Dynamical behaviors of equation 1 with $a = 2$, $b = 1$ and initial conditions $[0.1, 0, 0, 0]$: (a) average values of all variables, (b) Lyapunov exponents.

The symmetric attractors showcased in Figure 10 correspond to the parameter value $a = 2$, with two mirrored initial conditions utilized, IC1 = $[0.1, 0, 0, 0]$ shown in green and IC2 = $[-0.1, 0, 0, 0]$ illustrated in red while varying the parameter b. At $b = 3.5$, symmetric chaotic attractors are evident in the system, as seen in Figure 10a. As the parameter b increases to 4.3, the attractors exhibit a

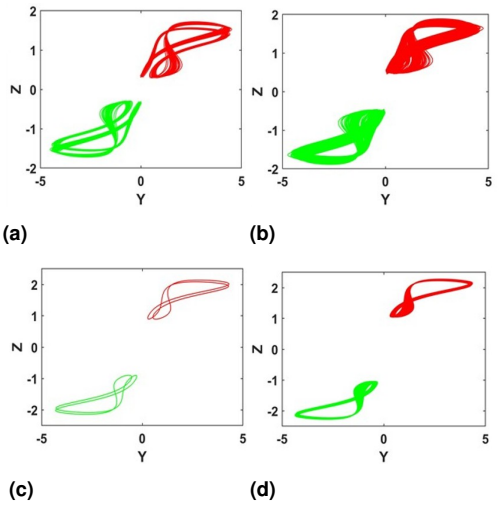

Figure 10 Coexisting symmetric attractors when $a = 2$ with initial condition IC1 = $[0.1, 0, 0, 0]$ (red), IC2 = $[-0.1, 0, 0, 0]$ (green): (a) $b = 3.5$, (b) $b = 4.3$, (c) $b = 6$, (d) $b = 6.7$.

more defined organizational structure, yet they continue to retain their chaotic characteristics as portrayed in Figure 10b. At $b = 6$, a significant transition in the system occurs, leading to periodic dynamics which is marked by the appearance of recurrent trajectories as illustrated in Figure 10c. Finally, at $b = 6.7$, the attractors attain further stabilization into symmetric periodic orbits as exhibited in Figure 10d. This figure adeptly highlights the evolution from chaotic behavior to periodic motion, concurrently sustaining symmetry as the parameter b is incrementally increased.

CIRCUIT IMPLEMENTATION

The purpose of this section is to conduct experiments in the actual world to verify theoretical results. The LM741CN operational amplifier, AD633JN multiplier, and monolithic ceramic capacitor have been employed to construct the chaotic system to validate the dynamical features of the chaotic oscillator. To facilitate meaningful comparisons, the values of the elements employed in the numerical analysis were preserved. Figure 11 illustrates the analog circuit corresponding to equation 1. The corresponding circuit state equations are articulated using Kirchhoff's law as follows:

$$\begin{cases} \dot{x} = \frac{R_{36}}{R_1 C_1}\left(\frac{-x\cdot y\cdot y}{R_{33}} + \frac{x}{R_{34}} + \frac{-z\cdot|w|}{100\cdot R_{36}} + \frac{V}{R_{37}}\right) \\ \dot{y} = \frac{R_{31}}{R_4 C_4}\left(\frac{-x}{R_{34}} + \frac{-y}{R_{23}} + \frac{x\cdot x\cdot y}{100\cdot R_{30}}\right) \\ \dot{z} = \frac{1}{R_7 C_2}x \\ \dot{w} = \frac{R_{21}}{R_{10} C_3}\left(\frac{w}{R_{18}} + \frac{-w\cdot|w|}{R_{19}} + \frac{z}{R_{20}}\right) \end{cases} \tag{8}$$

The circuit operates on a ±15V power supply. System (1) uses four state variables x, y, z, and w to describe the capacitors' state voltages across eight channels. Taking the 10kΩ resistor as a standard and setting the parameters $a = 2$ and $b = 1$, compute the appropriate parameters of the circuit elements. The parameter values are given as follows: $C_1 = C_2 = C_3 = C_4 = 1\,\text{nF}$, $R_6 = R_7 = R_9 = R_{10} = R_{11} = R_{12} = R_{13} = R_{14} = R_{15} = R_{17} = R_{18} = R_{19} = R_{20} = R_{21} = R_{22} = R_{31} = R_{32} = R_{37} = 10\,\text{k}\Omega$, $R_{23} = 5\,\text{k}\Omega$, $R_{30} = 50\,\Omega$, $R_{34} = 20\,\text{k}\Omega$, and $R_{33} = R_{35} = 500\,\text{k}\Omega$. Multisim 14.2 software was used to simulate the circuit, and Figure 12 shows the simulation outcomes. The odd attractors found

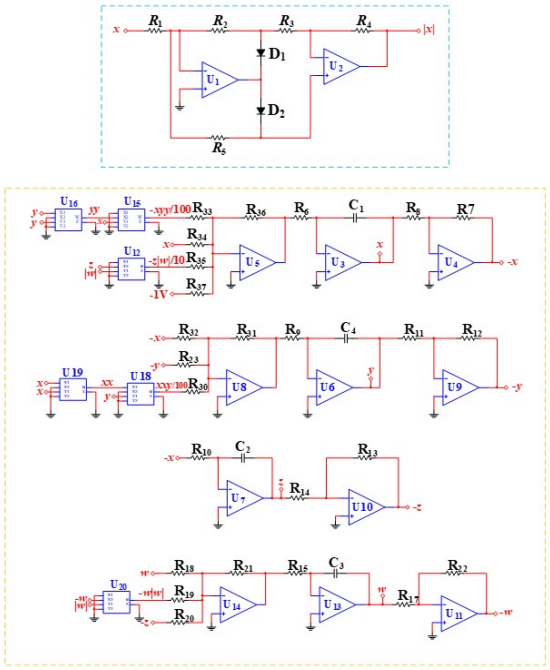

Figure 11 The chaotic oscillators modeling circuit.

in the analog circuit (Petrzela 2024) and the outcomes of the computer numerical simulation are essentially consistent (Kuznetsov *et al.* 2023b). There is some inaccuracy between the theoretical and actual findings due to the external environment and interruptions in precision.

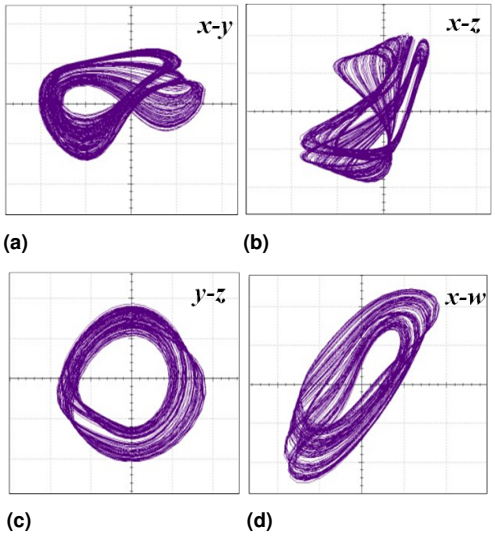

Figure 12 Circuit simulation of typical phase trajectories of equation 8 with $a = 2$, $b = 1$ under initial condition $[0.1, 0, 1, 0]$: (a) x-y plane, (b) x-z plane, (c) y-z plane, (d) x-w plane.

CONCLUSION

The investigation of the two-memristor chaotic system reveals the system's capability to generate complicated nonlinear dynamics such as symmetric bifurcation and multistability. This demonstrates that the system can be applied to secure communications,

adaptive control frameworks, and reconfigurable circuitry due to its system's intricate chaotic dynamics demonstrated by attractors, Lyapunov exponents, and bifurcation analysis. This work helps explain symmetric bifurcation and multistability by investigating the interplay of two memristors revealing how multiple attractors may exist and how chaotic behavior can be modulated. Although possessing numerous tantalizing properties, practical challenges, including experimental validation and noise robustness, as well as reconciling theoretical models with actual implementations need to be overcome to reach its full potential. This work sets the stage for further research into the design and realization of complex chaotic systems with improved functionality and robustness.

Availability of data and material

Not applicable.

Conflicts of interest

The authors declare that there is no conflict of interest regarding the publication of this paper.

Ethical standard

The authors have no relevant financial or non-financial interests to disclose.

LITERATURE CITED

Bao, H. *et al.*, 2022a Initial-condition effects on a two-memristor-based jerk system. Mathematics **10**: 411.

Bao, H. *et al.*, 2022b Parallel bi-memristor hyperchaotic map with extreme multistability. Chaos, Solitons & Fractals **160**: 112273.

Boya, B. *et al.*, 2022 The effects of symmetry breaking on the dynamics of an inertial neural system with a non-monotonic activation function: Theoretical study, asymmetric multistability, and experimental investigation. Physica A: Statistical Mechanics and its Applications **602**: 127458.

Chaintron, L.-P. and A. Diez, 2021 Propagation of chaos: a review of models, methods, and applications. ii. applications. arXiv preprint arXiv:2106.14812 .

Fang, S. *et al.*, 2022 Multistability phenomenon in signal processing, energy harvesting, composite structures, and metamaterials: A review. Mechanical Systems and Signal Processing **166**: 108419.

Fossi, J. *et al.*, 2023 Phase synchronization and coexisting attractors in a model of three different neurons coupled via hybrid synapses. Chaos, Solitons & Fractals **177**: 114202.

Guo, Q., N. Wang, and G. Zhang, 2021 A novel current-controlled memristor-based chaotic circuit. Integration **80**: 20–28.

Kamdem Tchiedjo, S. *et al.*, 2022 Dynamical behaviors of a chaotic jerk circuit based on a novel memristive diode emulator with a smooth symmetry control. The European Physical Journal Plus **137**: 940.

Kumari, U. and R. Yadav, 2023 Design and implementation of an efficient memristor-based chaotic circuit. International Journal of Information Technology **15**: 4449–4458.

Kuznetsov, A., Y. Sedova, and N. Stankevich, 2023a Coupled systems with quasi-periodic and chaotic dynamics. Chaos, Solitons & Fractals **169**: 113278.

Kuznetsov, N. *et al.*, 2023b Hidden attractors in chua circuit: mathematical theory meets physical experiments. Nonlinear Dynamics **111**: 5859–5887.

Lai, Q. *et al.*, 2023 Analysis and realization of a new memristive chaotic system with line equilibria and coexisting attractors. Journal of Vibration Engineering & Technologies **11**: 3493–3505.

Li, P. *et al.*, 2023 Dynamical properties of a meminductor chaotic system with fractal–fractional power law operator. Chaos, Solitons & Fractals **175**: 114040.

Li, P., R. Li, and C. Dai, 2021 Existence, symmetry breaking bifurcation and stability of two-dimensional optical solitons supported by fractional diffraction. Optics Express **29**: 3193–3210.

Lin, H. *et al.*, 2023 Memristor-coupled asymmetric neural networks: Bionic modeling, chaotic dynamics analysis and encryption application. Chaos, Solitons & Fractals **166**: 112905.

Luo, N. *et al.*, 2023 Well-defined double hysteresis loop in nanbo3 antiferroelectrics. Nature Communications **14**: 1776.

Marszalek, W., 2022 On physically unacceptable numerical solutions yielding strong chaotic signals. Entropy **24**: 769.

Masominia, A., 2024 *Neuro-inspired computing with excitable micro-lasers*. Ph.D. thesis, Université Paris-Saclay.

Penington, T., 2022 *A non-linear model and framework for implementing transformative change*. Ph.D. thesis, Victoria University.

Petrzela, J., 2024 Chaotic systems based on higher-order oscillatory equations. Scientific Reports **14**: 21075.

Silva-Juárez, A. *et al.*, 2021 Optimization of the kaplan-yorke dimension in fractional-order chaotic oscillators by metaheuristics. Applied Mathematics and Computation **394**: 125831.

Umar, T., M. Nadeem, and F. Anwer, 2024 Chaos-based image encryption scheme to secure sensitive multimedia content in cloud storage. Expert Systems with Applications **257**: 125050.

Wang, Q. *et al.*, 2024 A novel 4d chaotic system coupling with dual-memristors and application in image encryption. Scientific Reports **14**: 29615.

Wei, X. *et al.*, 2024 Nonlinear analysis, circuit design, and chaos optimization application of multiscroll chaotic attractors based on novel locally active non-polynomial memristor. Nonlinear Dynamics pp. 1–38.

Yang, F., J. Ma, and F. Wu, 2024 Review on memristor application in neural circuit and network. Chaos, Solitons & Fractals **187**: 115361.

How to cite this article: Khan, A., Li, C., Zhang, X., and Cen, X. A Two-memristor-based Chaotic System with Symmetric Bifurcation and Multistability. *Chaos and Fractals*, 2(1), 1-7, 2025.

ADBA Chaos and Fractals
Cutting-Edge Scientific Solutions

e-ISSN: 3023-8951
RESEARCH ARTICLE
Vol.2 / No.1 / 2025 / pp.8-13
https://doi.org/10.69882/adba.chf.2025012

FPGA-Based Chaotic Oscillator Designs and Performance Analysis

Muhammed Furkan Taşdemir *,1, **Murat Tuna** α,2 **and İsmail Koyuncu** β,3

*Institute of Natural and Applied Sciences, Afyon Kocatepe University, Afyonkarahisar, 03200, Türkiye, αDepartment of Electrical and Energy, Technical Sciences Vocational School, Kırklareli University, Kırklareli, 71000, Türkiye, βDepartment of Electrical Electronics Engineering, Faculty of Technology, Afyon Kocatepe University, Afyonkarahisar, 03200, Türkiye.

ABSTRACT Chaotic systems are highly sensitive to initial conditions, where even minute changes can result in vastly different outcomes. The non-linear nature of chaotic systems prevents them from reaching a stable state, instead exhibiting continuous change. This inherent unpredictability makes chaotic systems particularly valuable in fields such as cryptography, random number generation, and secure communications, where the need for complex and difficult-to-predict patterns is crucial. FPGA chips allow for hardware-level customization, enabling the optimization of chaotic systems for specific tasks. Implementing chaotic oscillators and systems on FPGA platforms facilitates efficient solutions for security-related applications, including encryption, pseudorandom number generation, and secure communication protocols. Additionally, the high-speed performance, low power consumption, and parallel processing capabilities of FPGAs make them ideal for implementing chaotic systems in industrial and commercial applications, where efficiency and security are paramount. One of the most basic structures used in real time chaos-based applications is chaotic oscillators. In this study, FPGA based chaotic oscillators presented in the literature have been examined according to important parameters such as maximum operating frequency of the designed system, chaotic oscillator type, application area and numerical methods used for designs and the results have been discussed.

KEYWORDS
Chaos
Chaotic oscillators
FPGA
Maximum operating frequency
Numerical methods

INTRODUCTION

Nonlinear systems are characterized by structures where nonlinearity and linearity are valid only within certain limits. Even seemingly simple or trivial behaviors in such systems can lead to unpredictable changes and outcomes. Within this spectrum, chaotic systems represent one of the most actively researched areas. Recently, chaotic systems have gained importance in addressing rising global security concerns. Advances in technology and economics have significantly increased the speed and volume of information exchange, leading to heightened security challenges. As large volumes of information are transmitted without loss, it becomes essential to store and encrypt data according to its application area. In this context, chaotic systems and the unique opportunities created by chaotic fluctuations play a pivotal role in solving these challenges. Unlike periodic systems, chaotic systems do not allow the prediction of future states, as they generate new values at each step, differing from previous values.

Chaotic systems find applications in diverse fields, including cybersecurity (Anees and H. 2018), voice and image processing (Litvinenko and A. 2019; Özkaynak and B. 2013; Barakat and S. 2013), Optimization algorithms (Gabr 2023), defense (Tanyıldızı and C. 2017), biomedical engineering (Vasyuta *et al.* 2019), and mechatronics (Huang and D. 2014). For instance, a study by Linsheng Zhang and colleagues developed an automation system transitioning from floating-point to fixed-point systems using Extreme Value Theory (Zhang and Z. 2009). Another study demonstrated synchronization between two chaotic systems based on the Vilnius chaotic oscillator, achieving consistent outcomes. Research introduced by Litvinenko explored chaotic systems like logistic, Bernoulli, and tent maps for DS-CDMA systems (Litvinenko 2017b). Further studies by Litvinenko and colleagues presented a Chaos Shift Keying (CSK) system using a modified Chua chaotic system, achieving synchronization between transmitters and receivers for data transmission (Litvinenko 2017a).

Similarly, M.K. Gabr implemented an encryption and decryption system utilizing Chua circuit-based chaos generators (Barakat and S. 2013). Chaotic systems, characterized by their sensitivity to initial conditions and complex nonlinear dynamics, have gained significant attention in recent years for applications such as secure communications, random number generation, and modeling natural phenomena. Among the platforms used to implement chaotic systems (Tasdemir *et al.* 2024) Field-Programmable Gate Arrays (FPGAs) stand out due to their high configurability, parallel processing capabilities, and real-time performance. This paper discusses the implementation of chaotic systems in FPGA chips,

Manuscript received: 16 January 2025,
Revised: 27 January 2025,
Accepted: 27 January 2025.

[1]mftasdemir@usr.aku.edu.tr (**Corresponding author**)
[2]murat.tuna@klu.edu.tr
[3]ismailkoyuncu@aku.edu.tr

comparing their advantages and challenges to alternative platforms such as Raspberry Pi, GPUs, and CPUs.

FPGAs excel in chaotic system modeling due to their inherent parallelism and hardware-level customization. Unlike CPUs and GPUs, FPGAs allow the direct mapping of mathematical models into hardware, enabling low-latency operations. For instance, the design of chaotic maps such as the Lorenz or logistic map can be efficiently implemented using digital logic blocks, which process data simultaneously rather than sequentially. Additionally, the power efficiency of FPGAs makes them particularly suitable for edge computing applications, where real-time chaotic systems are critical. However, the complexity of FPGA programming, often requiring expertise in hardware description languages (HDLs), remains a notable challenge (Taşdemir *et al.* 2020; Çevik *et al.* 2025). In contrast, Raspberry Pi serves as a low-cost, accessible alternative for chaotic system implementation. Its software-centric approach, relying on Python or C libraries, simplifies development but limits performance due to the sequential nature of its ARM-based CPU architecture.

While suitable for educational purposes and low-complexity models, it struggles with the computational demands of high-dimensional chaotic systems (Guillén-Fernández *et al.* 2022). Jetson GPUs, powered by NVIDIA's CUDA architecture, provide significant computational power for chaotic systems, especially in scenarios requiring high-dimensional data processing. Their massively parallel structure makes them ideal for simulations and research involving chaotic attractors or time-series analysis (Emin and Yaz 2023). However, GPUs typically consume more power than FPGAs and are less efficient for applications requiring low latency. Traditional CPUs, on the other hand, remain versatile for chaotic system studies. Despite their general-purpose design, modern multi-core processors can handle medium-complexity chaotic models efficiently.

CPUs are advantageous for prototyping and integrating chaotic systems into larger frameworks. Nevertheless, their sequential processing limits real-time performance compared to FPGAs or GPUs. FPGAs provide unparalleled flexibility and efficiency for chaotic system implementation, particularly in applications requiring low latency and energy efficiency. While platforms like Raspberry Pi, Jetson GPUs, and CPUs offer various benefits in terms of accessibility, computational power, or ease of development, their limitations make them less optimal for certain chaotic applications. As research in this field advances, hybrid systems that integrate the strengths of these platforms may emerge as a promising solution for complex chaotic system modeling. In the second part of the study, general information about FPGA chips has been given. In the Third Section, literature review results have been presented. In the last section, the results obtained from the studies have been evaluated.

FPGA CHIPS

FPGA chips are integrated circuits with semiconductor technology that allowing their internal structure may reconfigured and programmed according to the designer's requirements or the desired system. Advantages of FPGA chips include rapid prototyping (time-to-market), high speed and performance, flexibility, parallel signal processing, and low power consumption. These chips are widely utilized in various fields, including defense industries, cryptography, image and audio processing, artificial intelligence, satellite and radar communications, consumer electronics, and medical electronics. An example of a modern FPGA architecture is presented in Figure 1 (Xilinx 2017a). The basic FPGA architecture is sufficient for most applications and designs. In addition, modern FPGA architectures include many additional elements that increase computational density and efficiency. Examples of these structures include embedded memory for data storage (e-RAM/Block RAM), Phase-Locked Loops, high-speed serial transceivers, DSP48 Blocks, Soft/Hard processors, Gbit-level fast transceiver blocks.

FPGA chips are currently produced by leading companies such as AMD (Xilinx), Intel (Altera), Actel, Anadigm, Atmel, Leopard Logic, and Quick Logic using advanced technological processes. Instead of being offered solely as individual components, these chips are often integrated into FPGA development boards. These boards, which combine the FPGA chip with peripheral devices, power management systems, and programming/configuration infrastructures, provide significant advantages, including streamlined digital system design, prototyping, verification, and reduced time-to-market. Notably, manufacturers assign unique names to their chips to differentiate product lines. For instance, AMD categorizes its FPGA chips under names such as Artix, Kintex, and Virtex, each targeting different performance and application needs. As illustrated in Figure 2, the ML605 development board, featuring the Virtex-6 chip from Xilinx (now part of AMD), exemplifies a comprehensive solution for development and testing (Xilinx 2017b).

FPGA BASED CHAOTIC OSCILLATOR DESIGNS

One of the most basic structures used in real time chaos-based applications is chaotic oscillators. Considerable attention has been devoted in the literature to the FPGA-based modeling of chaotic oscillators. In a 2024 study, Sambas and colleagues introduced a novel 3D Jerk chaotic oscillator, which they implemented on the Virtex-6 ML605 FPGA chip. The design was developed in VHDL using a feedforward artificial neural network (ANN) model and adhered to the floating-point standard (32-bit IEEE-754-1985).

According to the findings, the maximum operating frequency of the proposed unit was determined to be 114.903 MHz. Additionally, the FPGA-based oscillator was utilized in applications such as pseudorandom number generation (PRNG) and image encryption, demonstrating its practical utility and versatility (Sambas *et al.* 2024b). In this study conducted in 2025, Moreira Bezerra and colleagues implemented both a discrete-space chaotic map and a chaotic image encryption scheme based on sequences generated using this map on an FPGA platform (Bezerra *et al.* 2025a). The study utilized two different FPGA architectures: the Altera Cyclone X 10CX105YF672E5G and the Xilinx Spartan 7 XC7S75FGGA676-1Q.

The researchers reported that the FPGA-implemented encryption scheme demonstrated lower resource utilization and power consumption compared to other proposed methods in the literature, highlighting its efficiency and practicality. In their study conducted in 2020, Hagras and colleagues developed an FPGA-based 4-D memristor chaotic oscillator design to implement a low-power, high-speed FPGA-based image encryption application (Hagras and Saber 2020). The design was implemented in a 32 fixed-point number format on the Xilinx Spartan-6 X6SLX45 board. The results demonstrated that the FPGA-based memristor chaotic system achieved a maximum operating frequency of 393 MHz, highlighting its efficiency and performance for real-time applications. Amdouni and colleagues implemented a chaos-based block cipher image encryption application using a 3D chaotic map oscillator on an FPGA platform (Amdouni *et al.* 2023).

The proposed approach introduced a robust chaos-based pseudorandom number generator (PRNG) relying on four 3D chaotic maps to generate high-quality keys. Additionally, to enhance the

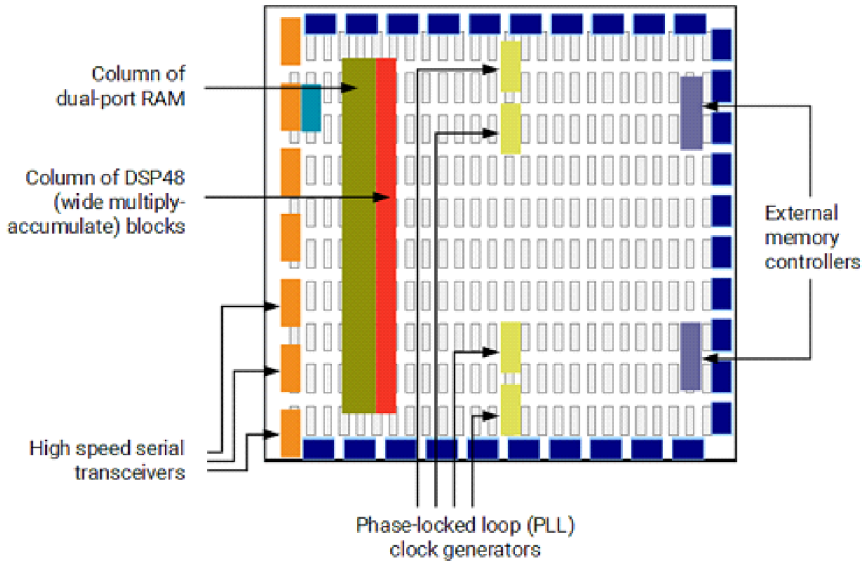

Figure 1 Modern FPGA structure

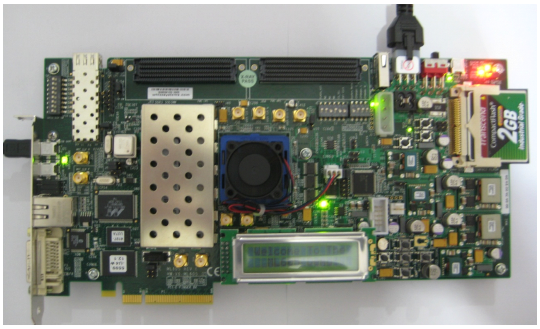

Figure 2 Xilinx/AMD ML605 development board

diffusion process and increase the complexity of the generated keys, the encryption process incorporated certain biological operations, such as DNA-based algebraic processes. The cryptosystem was implemented on the Xilinx ZedBoard Zynq Evaluation and Development Kit platform, achieving an operating frequency of 194.906 MHz. In a 2023 study, Gafsi and colleagues designed a robust cryptosystem for image encryption and decryption using high-quality keys and four different chaotic oscillators on the Xilinx FPGA-Zynq kit (Gafsi *et al.* 2023).

The system achieved an operating frequency of 142.8 MHz. The results of this study demonstrated that the system generated high-quality random number sequences, making it suitable for real-time applications, particularly for image encryption and decryption. Yu and colleagues presented a new approach in the literature by designing a 5D Memristive Hyperchaotic Sprott-C system on an FPGA platform (Yu *et al.* 2023b). Koyuncu and colleagues designed a 3D chaotic system using the 32-bit IQ-Math fixed-point number standard and the Euler numerical algorithm on an FPGA platform, implemented in VHDL (Koyuncu *et al.* 2020).

The system achieved an operating frequency of 464 MHz. Furthermore, they used the FPGA-based design to implement a true random number generator (TRNG) application with a dual entropy core. Another study published in 2019, Alçın and colleagues designed a high-speed true random number generator (TRNG) using a 3D chaotic system and artificial neural networks on an FPGA kit, implemented in VHDL (Alcin *et al.* 2019). The system achieved an operating frequency of 231.616 MHz. The results demonstrated that the designed system could provide high operating frequencies and high-quality random bit sequences, making it suitable for a wide range of embedded cryptographic applications. This study introduces a novel hardware implementation of Artificial Neural Networks (ANNs) for modeling the Pehlivan–Uyaroglu Chaotic System (PUCS) on a FPGA. The research is divided into two main sections. Initially, a 3-8-3 Feed Forward Neural Network (FFNN) was developed and trained using the back propagation algorithm in Matlab R2015a, achieving high precision.

Subsequently, the trained FFNN was implemented in hardware using VHDL on a Xilinx Virtex 6 (XC6VCX240T) chip. The implementation employs IEEE 754 single-precision floating-point format and the Xilinx CORDIC algorithm for approximating the Log-Sigmoid transfer function. Operating at a clock frequency of up to 266.429 MHz, the design demonstrates the feasibility of modeling chaotic systems with ANNs on FPGA (Alcin *et al.* 2016). Koyuncu *et al.* (2019) focuses on the implementation of the 5-D hyperchaotic Lorenz system on an FPGA using the Heun algorithm to enhance chaos-based embedded engineering applications. The design employs the 32-bit IEEE-754-1985 floating-point format and is coded in VHDL. The FPGA-based system achieves a maximum operating frequency of 430.146 MHz. Additionally, the system is realized as a physical circuit using analog components. Comparative analysis between FPGA-based results and computer-based numerical simulations was conducted, with error metrics

Table 1 Comparison of Chaotic Generator Implementations on FPGA Platforms

Study	Chaotic Generator	Platform	Max. Freq. (MHz)	Numerical Method	Application
(Tasdemir *et al.* 2024)	Modified Chua	Xilinx Virtex-6	273.631–50.242	Forward Euler	–
(Sambas *et al.* 2024b)	New 3-D Jerk Oscillator	Xilinx Virtex-6	114.903	ANN	PRNG, Image Encryption
(Bezerra *et al.* 2025a)	Discrete-Space Chaotic Map	Altera Cyclone X	474	Fractional Order	Image Encryption
(Hagras and Saber 2020)	4-D Memristor Chaotic Oscillator	Xilinx Spartan-6	393	RK4	PRNG, Image Encryption
(Amdouni *et al.* 2023)	3D Chaotic Oscillator	Xilinx Zed Board	194.906	XSG-Xilinx System Generator	PRNG, Block-Cipher Encryption
(Gafsi *et al.* 2023)	3D Chaotic Oscillator	Xilinx FPGA-Zynq	142.8	XSG-Xilinx System Generator	Image Encryption, Decryption
(Yu *et al.* 2023b)	5D Memristive HC Sprott-C	Xilinx FPGA	–	RK4	–
(Koyuncu *et al.* 2020)	3D Chaotic Oscillator	Xilinx Virtex-6	464	Euler	TRNG
(Alcin *et al.* 2019)	3D Chaotic Oscillator	Xilinx Virtex-6	231.616	ANN	TRNG
(Alcin *et al.* 2016)	Pehlivan–Uyaroglu	Xilinx Virtex-6	266.429	FFNN	TRNG
(Koyuncu *et al.* 2019)	5-D Hyperchaotic Lorenz	Xilinx Virtex-6	430.146	Heun	MSE
(Sambas *et al.* 2022)	3D Chaotic System	Xilinx Virtex-6	462.731	Euler	PRNG
(Tuna *et al.* 2019)	Lü-Chen CO	Xilinx Virtex-6	464.688	Heun	–
(Zourmba *et al.* 2025)	1D CO	Altera Cyclone-III	50	–	Image Encryption
(Kemdoum *et al.* 2024)	Perturbed Chen	Xilinx Nexys 4	113	XSG-Xilinx System Generator	PRNG and Encryption
(Rodríguez-Muñoz *et al.* 2024)	7 Lorenz-Type Oscillators	Altera Cyclone II	50.69	Forward Euler	–
(Bonny *et al.* 2024)	Switching-Type Oscillator	Altera Cyclone IV	100	Euler	Image Encryption
(Gonzalez *et al.* 2025)	Multiscroll Chaotic Network	Altera DE1	33.83	Euler	PRNG
(Capligns *et al.* 2025)	Modified Chua	Intel Cyclone V	50	Simulink-Forward Euler	Communication
(Li *et al.* 2025)	Novel 3D-PCHCS	Altera Cyclone IV	50	Euler	Encryption
(Bezerra *et al.* 2025b)	Discrete-Space Chaotic Map	Xilinx Spartan 7	473.78	Euler-RK4	Image Encryption
(Yu *et al.* 2023a)	Memristive Oscillator	Altera Cyclone IV	–	Euler Method	Flux Control Synchronization
(Sambas *et al.* 2024a)	Hyperjerk Oscillator	Xilinx Zybo Z7-20	111	Forward Euler	Image Encryption
(Wang *et al.* 2022)	Fractional-Order Colpitts	Altera Cyclone IV	72.06	Multi-Step FDTM	–

such as Mean Squared Error (MSE) and Root Mean Squared Error (RMSE) evaluated. This work highlights the potential for FPGA implementation in chaos-based engineering applications.

Sambas *et al.* (2022) introduces a novel three-dimensional chaotic system with line equilibrium and explores its dynamic properties, including Lyapunov exponents, phase portraits, equilibrium points, bifurcation diagrams, multistability, and coexisting attractors. Synchronization results based on integral sliding mode control (ISMC) are derived for the system, and an electronic circuit implementation is presented, demonstrating strong agreement between theoretical Matlab simulations and MultiSim results. The study also implements an FPGA-based PRNG using the chaotic

system, achieving a throughput of 462.731 Mbps and passing all NIST-800-22 randomness tests. Additionally, an image encryption algorithm combining pixel-level scrambling, bit-level scrambling, and pixel value diffusion is proposed. Experimental results show the algorithm effectively resists brute force and differential attacks by shuffling pixel positions and altering pixel values.

Tuna *et al.* (2019) focuses on a 3D chaotic system without equilibrium points, an emerging area in chaotic system research, with potential applications, particularly in encryption. The system, lacking homoclinic and heteroclinic orbits, was examined, and its electronic circuit implementation was completed, yielding phase portraits via oscilloscope outputs. The system was also modeled on LabVIEW Field Programmable Gate Array (FPGA), with FPGA chip statistics and outputs analyzed. Additionally, using VHDL and the RK-4 algorithm, a new FPGA-based chaotic oscillator design was developed. Comparative analysis of LabVIEW-based and VHDL-based designs was conducted using the Xilinx ISE Simulator. A novel chaos-based Random Number Generator (RNG) was created, passing FIPS-140-1 and NIST-800-22 randomness tests. Finally, the RNG was applied to video encryption, with security analyses confirming its robustness.

In other paper investigates the design and implementation of the Modified Chua chaotic oscillator on FPGA using fixed-point and floating-point number representations, comparing their performances. The Euler numeric algorithm was employed to design the oscillator. Initially, the fixed-point version was modeled in MATLAB Simulink and converted to VHDL using the MATLAB HDL Coder Toolbox. Subsequently, the floating-point version was directly designed with VHDL. Both versions were tested and synthesized for the Virtex-6 FPGA on the ML605 development board using Xilinx ISE Design Tools 14.2. The results revealed that the fixed-point representation achieved a maximum operating frequency of 50.242 MHz, whereas the floating-point representation reached 273.631 MHz. This demonstrates the performance trade-offs between the two number standards in chaotic oscillator implementations (Tasdemir *et al.* 2024).

With the study implements the autonomous Lü-Chen (2002) chaotic system on an FPGA using the Heun numerical algorithm in VHDL with a 32-bit IQ-Math fixed-point format to support chaos-based embedded engineering applications. Core components like multipliers, adders, and subtractions, compatible with the fixed-point standard, were created using the Xilinx IP CORE Generator. The design was simulated, synthesized, and tested on a Virtex-6 FPGA chip, with chip statistics, phase portraits, and Place and Route results presented. The FPGA-based design achieves a maximum operating frequency of 464.688 MHz, the highest reported in the literature for such systems, and exhibits superior resource utilization compared to other 3D FPGA-based chaotic oscillators. Accuracy was validated through Mean Square Error (MSE) and Root Mean Square Error (RMSE) analyses, confirming its reliability. The study demonstrates that the hardware-based Lü-Chen chaotic oscillator is highly effective for applications like cryptography, secure communication, and random number generation (Zourmba *et al.* 2025). FPGA-based chaotic oscillators in literature have been given in the Table 1.

CONCLUSION

This study provides a comprehensive review of chaotic systems implemented on FPGA chips, highlighting their various features and characteristics. These features, including application domains, numerical systems, maximum operating frequency, target devices, and applied methodologies, are systematically presented in a detailed table. The research incorporates advanced numerical methods and computational techniques, such as artificial neural networks, fourth-order Runge-Kutta (RK4), fractional-order calculations, Heun's method, Euler's method, and Xilinx System Generator (XSG). Notably, a system designed using the Altera Cyclone X 10CX105YF672E5G FPGA chip, based on the discrete-space chaotic map numerical method, achieved a maximum operating frequency of 474 MHz. This performance highlights the potential of FPGA-based chaotic systems in high-speed and computationally demanding applications. The study not only emphasizes the technical advantages of these implementations but also contributes to the growing body of literature on the efficient utilization of chaotic systems on FPGA chips for various real-world and industrial applications.

Availability of data and material

Not applicable.

Conflicts of interest

The authors declare that there is no conflict of interest regarding the publication of this paper.

Ethical standard

The authors have no relevant financial or non-financial interests to disclose.

LITERATURE CITED

Alcin, M., I. Koyuncu, M. Tuna, M. Varan, and I. Pehlivan, 2019 A novel high speed artificial neural network–based chaotic true random number generator on field programmable gate array. International Journal of Circuit Theory and Applications **47**: 365–378.

Alcin, M., I. Pehlivan, and I. Koyuncu, 2016 Hardware design and implementation of a novel ann-based chaotic generator in fpga. Optik **127**: 5500–5505.

Amdouni, R., M. Gafsi, and N. Abbassi, 2023 Robust hardware implementation of a block-cipher scheme based on chaos and biological algebraic operations. Multimedia Tools and Applications **82**: 37097–37130.

Anees, A. and I. H., 2018 A novel method to identify initial values of chaotic maps in cybersecurity. MDPI .

Barakat, M. L. and A. S., 2013 Hardware stream cipher with controllable chaos generator for colour image encryption. IETL .

Bezerra, J. I. M., G. Machado, and R. I. Soares, 2025a Fpga implementation of low cost and low power chaotic encryption scheme based on a discrete-space chaotic map. Multimedia Tools and Applications .

Bezerra, J. I. M., G. Machado, R. I. Soares, V. V. de Almeida Camargo, and A. Molter, 2025b Fpga implementation of low cost and low power chaotic encryption scheme based on a discrete-space chaotic map. Multimedia Tools and Applications pp. 1–22.

Bonny, T., F. AlMutairi, and W. A. Nassan, 2024 A novel clock-glitch-attack-proof image encryption algorithm implemented on fpga. Multimedia Tools and Applications **83**: 18881–18906.

Capligns, F., R. Babajans, D. Cirjulina, D. Kolosovs, and A. Litvinenko, 2025 Frequency-modulated antipodal chaos shift keying chaotic communication on field program gate array: Prototype design and performance insights. Applied Sciences **15**: 1156.

Emin, B. and M. Yaz, 2023 Digital implementation of chaotic systems using nvidia jetson agx orin and custom dac converter. Unpublished .

Gabr, M. K., 2023 Image encryption based on base-n prngs key application and parallel base-n s-boxes. The German University, Cairo .

Gafsi, M., M. A. Hajjaji, and J. Malek, 2023 Fpga hardware acceleration of an improved chaos-based cryptosystem for real-time image encryption and decryption. Journal of Ambient Intelligence and Humanized Computing **14**: 7001–7022.

Gonzalez, J. A. G., J. de Jesus Rangel-Magdaleno, and J. M. Munoz-Pacheco, 2025 Fpga implementation of a multi-prng based on a multiscroll chaotic hopfield neural network. IEEE Transactions on Industrial Informatics .

Guillén-Fernández, O., E. Tlelo-Cuautle, L. G. de la Fraga, Y. Sandoval-Ibarra, and J.-C. Nuñez-Perez, 2022 An image encryption scheme synchronizing optimized chaotic systems implemented on raspberry pis. Mathematics **10**: 1907.

Hagras, E. A. A. and M. Saber, 2020 Low power and high-speed fpga implementation for 4d memristor chaotic system for image encryption. Multimedia Tools and Applications **79**: 23203–23222.

Huang, Z. and W. D., 2014 Similarity measure between patient traces for clinical pathway analysis: Problem, method, and applications. IEEE Journal of Biomedical and Health Informatics pp. 4–14.

Kemdoum, F. N., J. R. M. Pone, M. Bajaj, S. R. D. Naoussi, G. P. A. Kuete, *et al.*, 2024 Fpga based implementation of a perturbed chen oscillator for secure embedded cryptosystems. Scientific Reports **14**: 21262.

Koyuncu, I., M. Alcin, M. Tuna, I. Pehlivan, M. Varan, *et al.*, 2019 Real-time high-speed 5-d hyperchaotic lorenz system on fpga. International Journal of Computer Applications in Technology **61**: 152–165.

Koyuncu, I., M. Tuna, I. Pehlivan, C. B. Fidan, and M. Alçın, 2020 Design, fpga implementation and statistical analysis of chaos-ring based dual entropy core true random number generator. Analog Integrated Circuits and Signal Processing **102**: 445–456.

Li, S. Y., G. Y. Wu, J. Y. Sun, P. F. Yan, and H. Zhang, 2025 Novel 3d-pchcs design and application on ophthalmic medical image copyright protection with fpga implementation. Journal of Real-Time Image Processing **22**: 1–15.

Litvinenko, A., 2017a *Use of Chaotic Sequences For Data Transmission System*. Ph.D. thesis, Riga Technical University.

Litvinenko, A., 2017b *Use of Chaotic Sequences for Data Transmission Systems*. Ph.D. thesis, Riga Technical University, Faculty of Electronics and Telecommunications, Institute of Radioelectronics.

Litvinenko, A. and A. A., 2019 Advanced chaos shift keying based on a modified chua's circuit. In *2019 IEEE Microwave Theory and Techniques in Wireless Communications (MTTW)*, pp. 17–22.

Rodríguez-Muñoz, J. D., J. D. Tavizón-Aldama, and E. Tlelo-Cuautle, 2024 Experimental observation of chaotic attractors from the fpga implementation of 3d chaotic systems. IETE Journal of Education **65**: 6–14.

Sambas, A., M. Miroslav, S. Vaidyanathan, B. Ovilla-Martínez, E. Tlelo-Cuautle, *et al.*, 2024a A new hyperjerk system with a half line equilibrium: Multistability, period doubling reversals, antimonotonicity, electronic circuit, fpga design, and an application to image encryption. IEEE Access **12**: 9177–9194.

Sambas, A., S. Vaidyanathan, X. Zhang, I. Koyuncu, T. Bonny, *et al.*, 2022 A novel 3d chaotic system with line equilibrium: Multistability, integral sliding mode control, electronic circuit, fpga implementation and its image encryption. IEEE Access **10**: 68057–68074.

Sambas, A., X. Zhang, and I. A. R. Moghrabi, 2024b Ann-based chaotic prng in the novel jerk chaotic system and its application for the image encryption via 2-d hilbert curve. Scientific Reports **14**: 29602.

Tanyıldızı, E. and T. C., 2017 Kaotik haritalı balina optimizasyon algoritmaları. Science and Engineering Journal of Fırat University pp. 307–317.

Tasdemir, M. F., A. Litvinenko, I. Koyuncu, and F. Capligins, 2024 Performance evaluation of fpga-based design of modified chua oscillator. Chaos Theory and Applications **6**: 249–256.

Taşdemir, M. F., I. Koyuncu, E. Coşgun, and F. Katırcıoglu, 2020 Real-time fast corner detection algorithm based image processing application on fpga. In *International Asian Congress on Contemporary Sciences-III*, pp. 1–6, IKSAD Publishing.

Tuna, M., M. Alcin, I. Koyuncu, C. B. Fidan, and I. Pehlivan, 2019 High speed fpga-based chaotic oscillator design. Microprocessors and Microsystems **66**: 72–80.

Vasyuta, K., F. Zots, and I. Zakharchenko, 2019 Building the air defense covert information and measuring system based on orthogonal chaotic signals. Peer-Reviewed Open Access Scientific Journal pp. 33–43.

Wang, H., D. Zhan, X. Wu, and S. He, 2022 Dynamics of a fractional-order colpitts oscillator and its fpga implementation. The European Physical Journal Special Topics **231**: 2467–2476.

Xilinx, 2017a Sdaccel documentation. https://www.xilinx.com/htmldocs/xilinx2017_4/sdaccel_doc/odz1504034293215.html.

Xilinx, 2017b Xilinx virtex-6 ml605 development board. https://www.xilinx.com/products/boards-and-kits/ek-v6-ml605-g.html.

Yu, F., W. Zhang, X. Xiao, W. Yao, S. Cai, *et al.*, 2023a Dynamic analysis and fpga implementation of a new, simple 5d memristive hyperchaotic sprott-c system. Mathematics **11**: 701.

Yu, F., W. Zhang, X. Xiao, W. Yao, S. Cai, *et al.*, 2023b Dynamic analysis and fpga implementation of a new, simple 5d memristive hyperchaotic sprott-c system. Mathematics **11**: 701.

Zhang, L. and Y. Z., 2009 Floating-point to fixed-point transformation using extreme value theory. In *Eighth IEEE/ACIS International Conference on Computer and Information Science*, pp. 271–276.

Zourmba, K., J. Y. Effa, C. Fischer, J. D. Rodríguez-Muñoz, M. F. Moreno-Lopez, *et al.*, 2025 Fractional order 1d memristive time-delay chaotic system with application to image encryption and fpga implementation. Mathematics and Computers in Simulation **227**: 58–84.

Çevik, G., B. Sarıoğlu, and B. Aka, 2025 Fpga implementation of an optimized neural network for cfd acceleration. AEU-International Journal of Electronics and Communications **188**: 155574.

Özkaynak, F. and A. B., 2013 Security analysis of an image encryption algorithm based on chaos and dna encoding. IEEE .

How to cite this article: Tasdemir, M. F., Tuna, M., and Koyuncu, I. FPGA-Based Chaotic Oscillator Designs and Performance Analysis. *Chaos and Fractals*, 2(1), 8-13, 2025.

ADBA Chaos and Fractals
Cutting-Edge Scientific Solutions

e-ISSN: 3023-8951
RESEARCH ARTICLE
Vol.2 / No.1 / 2025 / pp.14-19
https://doi.org/10.69882/adba.chf.2025013

Permanent Magnet Synchronous Motor with Load Torque: Dynamics, Circuitry Execution and Control

Rolande Tsapla Fotsa[*,1], **Paloma Kevina Koubeu Papemsi**[α,2], **Gideon Pagnol Ayemtsa Kuete**[β,γ,3], **Justin Roger Mboupda Pone**[γ,4], **Serge Raoul Dzonde Naoussi**[Γ,5], **Foutse Momo**[ς,6] **and Pierre Ele**[ψ,7]

[*]Department of Mechanical Engineering, College of Technology, University of Buea, P.O. BOX 63 Buea, Cameroon, [α]Rousseau Higher Institute, University of Douala, P.O. Box 2701, Douala, Cameroon, [β]Laboratory of Energy and Electrical and Electronic Systems, Department of Physics, Faculty of Science, University of Yaounde I, P.O. Box 812, Yaounde, Cameroon, [γ]Research Unit of Automation and Applied Computer (RU-AIA), Electrical Engineering Department of IUT-FV, University of Dschang, P.O. Box: 134, Bandjoun, Cameroon, [Γ]Technology and Applied Sciences Laboratory (TASL), University Institute of Technology of Douala (IUT of Douala), University of Douala, Post Box 8698, Douala, Cameroon, [ς]Biomedical Engineering, Energy and Modeling Laboratory (BEEMo.Lab.), Higher Institute of Science and Technology (HIST), University of Mountains, P.O. Box 208, Bangangte, Cameroon, [ψ]Electrical and Engineering, Telecommunications Department, National Advanced School of Engineering, University of Yaounde I, P.O. Box 812, Yaounde, Cameroon.

ABSTRACT This paper is interested in the study of the dynamics and control of the permanent magnet synchronous motor with load torque (PMSMLT). PMSMLT has three fixed points where one is saddle and the two others are saddle focus. PMSMLT exhibits no oscillations, periodic characteristics, chaotic characteristics and coexistence between no oscillations and chaotic characteristics. In order to validate the results obtained numerically, an electronic implementation of PMSMLT is performed in probe simulation program with integrated circuit emphases (PSPICE) environment which reveals a concordance between the numerical simulations and the experimental verifications. The coexisting characteristics is eliminated by the linear augmentation control method.

KEYWORDS
Permanent magnet synchronous motor
Load torque
Chaos
Coexisting characteristics
Linear augmentation control
Implementation circuit

INTRODUCTION

Rotating machines are electrical systems intended for the majority to control industrial systems linked to their mechanization (Wildi 2006; Chapman 2005; Santoso and Beaty 2018). These machines are classified into two main categories depending on their use. There are direct current machines and alternating current machines. Due to its relatively simple control, DC machines are increasingly used and considered as electric actuators for motorizing multiple engineering applications such as high-speed trains, elevators, drones, crushing mills, etc. (Fitzgerald *et al.* 1991; Wildi 2006; Borisavljevic 2013). The synchronous machine in most cases is used in three phases. It behaves as a reversible electromechanical energy converter. Thus, it can operate in motor mode or in generator mode depending on the voltage: In motor operation, the electrical energy provided by the source is transformed into mechanical energy and in generator or alternator operation, the mechanical energy is transformed into redirected electrical energy towards the source (Say and Taylor 1980; Hughes 2006; El-Sharkawi 2000). In generator operation, the synchronous motor can redirect the electrical energy. This application finds opportunities in wind turbines for the production of electricity, thanks to the possibility of providing reactive energy by modulating the excitation current. The synchronous machine in alternator operation can be used in power plants for the conversion of mechanical energy into electrical energy (Chau and Wang 2011; Machowski *et al.* 2012; Leine and Nijmeijer 2004).

The synchronous machine consists of a rotating part and a fixed part, the two separated by an air gap. The rotor, which is the rotating part of the synchronous machine, can consist of permanent magnets or consist of a winding powered by direct current and a magnetic circuit (electromagnet). Permanent magnet synchronous motors (PMSM) have advantages and applications in the automotive sector: lower inertia and weight than those with a wound rotor, improved efficiency thanks to the absence of consumption in the rotor, and reduced maintenance due to the

Manuscript received: 21 January 2025,
Revised: 28 January 2025,
Accepted: 29 January 2025.

[1]rtsapla@yahoo.com (**Corresponding author**)
[2]palilomapapemsi@gmail.com
[3]pagnolayimtsa@gmail.com
[4]mboupdapone00@gmail.com
[5]sdzonde@gmail.com
[6]mfoutse@yahoo.fr
[7]pierre.ele@univ-yaounde1.cm

absence of brooms (Iqbal and Singh 2019; Cheukem *et al.* 2020; Hua *et al.* 2022). Several works have already been carried out on PMSM. This work essentially focuses on the search for chaos in the machine and the control of undesirable dynamic states such as chaos (Donglian *et al.* 2005; Luo 2014; Luo *et al.* 2014). In the mathematical model of PMSMs proposed in the literature, the authors do not consider the saliency ratio, which is very low. However, it should be noted that a low saliency ratio has a negative impact on the machine in the sense that the power factor (which increases with the saliency ratio) of the electrical installation will be very low, thus resulting in a lower active power developed by the very weak motor, which favors a very high current which, from an economic point of view, generates losses for the user. Furthermore, we note that the work on PMSMs was carried out when they are empty, that is to say, the load torque is zero (Maeng and Choi 2013; Vadivel *et al.* 2023; Yamdjeu *et al.* 2024; Mao and Liu 2019; Du-Qu and Bo 2009).

In light of what was presented earlier, it appears that the literature still remains vague on the behavior of PMSMLT (TL $\neq 0$: continuous or discrete variable). It would therefore be interesting to fully study these motors in the presence of load torque because in reality, a motor is made to be used and therefore cause a movement. The objective of this paper is to study the dynamics of a PMSMLT in the presence of mechanical load torque and to carry out its control in order to make it operate in the manner desired by the user. To carry out this paper, it is structured into four sections. The first section presents the introduction. Section two is devoted to the dynamic analysis of PMSMLT and its electronic implementation. Section three presents the control of unwanted dynamic states. The paper ends with a conclusion in section 4.

THEORETICAL ANALYSIS OF PMSMLT AND ITS ELECTRONIC IMPLEMENTATION

The PMSMLT is described by the set of equations (Cheukem *et al.* 2020):

$$\frac{dx}{dt} = -x + yz, \tag{1a}$$

$$\frac{dy}{dt} = -y - xz + \gamma z, \tag{1b}$$

$$\frac{dz}{dt} = \sigma(y - z) + T_L, \tag{1c}$$

where x and y are the dimensionless direct and quadrature currents, respectively, z the angle speed, T_L the dimensionless load torque and σ, γ are the system parameters. System (1) is invariant under the coordinate transformation $(x, y, z)(x, -y, -z)$. The PMSMLT is dissipative because $\nabla V = \frac{\partial \dot{x}}{\partial x} + \frac{\partial \dot{y}}{\partial y} + \frac{\partial \dot{z}}{\partial z} = -(2 + \sigma)$. The fixed points of PMSMLT are obtained by solving the system of equation $\dot{x} = \dot{y} = \dot{z} = 0$ which gives

$$x = z\left(z - \frac{T_L}{\sigma}\right) \tag{2a}$$

$$y = \frac{T_L}{\sigma} + z \tag{2b}$$

$$\sigma z^3 - T_L z^2 - (\gamma - 1)\sigma z - T_L = 0 \tag{2c}$$

Equation 2c admits fixed points whose number varies depending on the values of the torque T_L and the parameter σ. Using a digital calculator as well as the fixed values of the parameters ($\sigma = 4.56$; $\gamma = 20$; $T_L = 6.5$), three fixed points are obtained:

$$\begin{aligned} E_1 &= (0.1132, -1.5009, -0.0754), \\ E_{2,3} &= (19.2762, \pm 3.7352, \pm 5.1606). \end{aligned} \tag{2}$$

The stability of the system for each fixed point is determined by the evaluation of the eigenvalues of the Jacobian matrix

$$J = \begin{bmatrix} -1 & z & y \\ -x & -1 & -x + \gamma \\ 0 & \sigma & -\sigma \end{bmatrix}. \tag{4}$$

The characteristic equation corresponding to the first fixed point E_1 obtained using $\det(J - \lambda I) = 0$ is given by:

$$\begin{aligned} \lambda^3 + (\sigma + 2)\lambda^2 + (2\sigma + 0.1132\sigma + \gamma\sigma + 1.0056)\lambda \\ + \sigma(0.7679 - \gamma) = 0. \end{aligned} \tag{5}$$

The eigenvalues, the fixed points $E_{1,2,3}$ are presented in Table 1. Table 1 reveals that the fixed point E_1 is a saddle while the fixed points $E_{2,3}$ are saddle focus.

Table 1 Eigenvalues of fixed points $E_{1,2,3}$.

Eigenvalues	E_1	$E_{2,3}$
λ_1	-0.9940	$-0.0586 + 5.7173i$
λ_2	6.9039	$-0.0586 + 5.7173i$
λ_3	-12.4698	-6.4420

Numerical analysis of PMSMLT

In order to know the influence of the load torque and other parameters on the dynamical behaviours of PMSMLT, the 2D largest Lyapunov exponent (LLE) are illustrated in Figure 1.

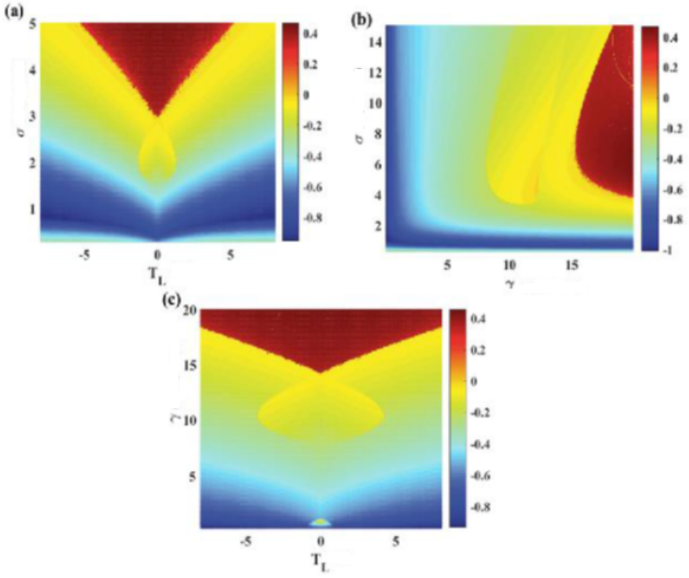

Figure 1 2D LLE in the planes: (a) (T_L, σ) with $\gamma = 20$, (b) (γ, σ) with $T_L = 2.0$, and (c) (T_L, γ) avec $\sigma = 8$ for the initial conditions $(x_0, y_0, z_0) = (0.01, 0.01, 0.01)$.

Figure 1 makes it possible to distinguish between chaotic zones (for positive LLE) and periodicity zones (for negative LLE) depending on the system parameters. Figure 2 represents the phase portrait of the chaotic state for fixed values of the system parameters.

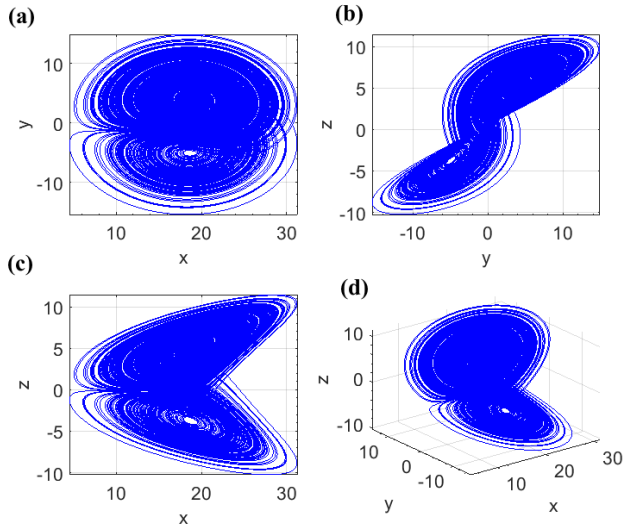

Figure 2 Phase portraits following the planes: (a) $(x$-$y)$, (b) $(y$-$z)$, (c) $(x$-$z)$, and (d) (x, y, z) for the following parameter values: $\sigma = 4.56$, $\gamma = 20$, $T_L = 6.5$ obtained for the initial conditions $(x_0, y_0, z_0) = (0.01, 0.01, 0.01)$.

Figure 2 shows the chaos encountered in the PMSMLT. Figure 3 presents the forward (in black) and return (in red) bifurcation diagrams of the PMSMLT forward current as well as their graphs of the corresponding LLE as a function of the T_L load torque.

The coexistence between chaos and no oscillations is observed in Figure 3 for the torque values between $6.448 \leq T_L \leq 5.824$ on the one hand and $5.824 \leq T_L \leq 6.448$ on the other hand. In order

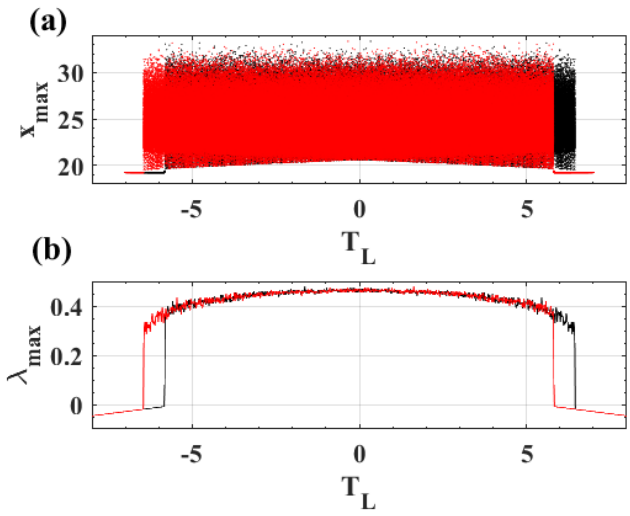

Figure 3 Bifurcation diagram showing the local maxima of x of the PMSMLT as a function of T_L load as well as the graph of the corresponding LLE for $\sigma = 4.56$ and $\gamma = 20$. The graphs in black represent the forward digraphs, and those in red represent the return.

to find the initial conditions leading to coexisting attractors, the drawing of the basin of attraction is carried out in Figure 4 by considering the parameter values leading to coexistence and the initial conditions are varied in the plane (x_0, y_0).

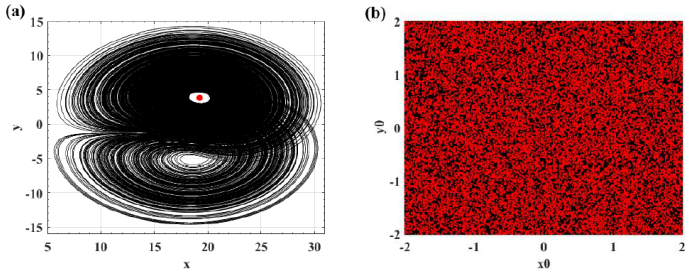

Figure 4 (a) Phase portrait in the plane (x, y) and (b) basin of attraction following the plane (x_0, y_0) putting for $\sigma = 5.46$, $\gamma = 20$, $T_L = 6.5$. The black lines are obtained using the initial conditions $(x_0, y_0, z_0) = (0, 0, 0)$, while the red lines are obtained using the initial conditions $(x_0, y_0, z_0) = (0, 0.2, 0)$.

Figure 4(a) shows the coexistence between chaos and the fixed point obtained respectively by the initial conditions $(x_0, y_0, z_0) = (0, 0, 0)$ and $(x_0, y_0, z_0) = (0, 0.2, 0)$. The set of initial conditions in Figure 4(b) leads to the chaotic attractor and a fixed point.

Electronic implementation of PMSMLT

The electronic implementation of PMSMLT on PSPICE software was done to verify the results found during the numerical simulations of PMSMLT. The advantages of electronic implementation include reduced costs and energy consumption, enhancing their performance and reliability. The electronic circuit diagram of the PMSMLT is given in Figure 5.

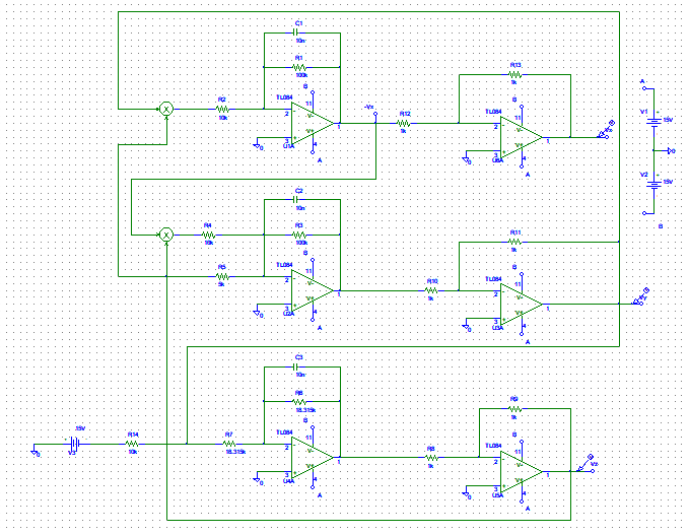

Figure 5 Circuit of the electronic implementation of the PMSMLT.

Figure 5 includes six operational amplifiers, two analog multipliers, three capacitors, fourteen resistors, a 15 V voltage source, and a symmetrical power supply of ±15 V. The phase portraits in Figure 6 are obtained from PSPICE.

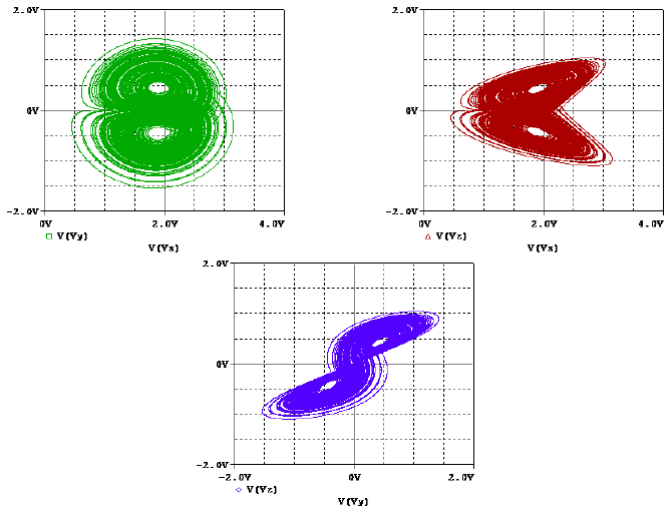

Figure 6 Phase portraits under PSPICE showing the chaotic behavior in the MSAP under load obtained for the resistance value $R_{14} = 10$ kΩ corresponding to the chaotic attractor. The other component values are $R_2 = R_4 = 10$ kΩ; $R_5 = 5$ kΩ; $R_1 = R_3 = 100$ kΩ; $R_8 = R_9 = R_{10} = R_{11} = R_{12} = R_{13} = 1$ kΩ; $R_6 = R_7 = 18.315$ kΩ, and $C_1 = C_2 = C_3 = 10$ nF. The initial conditions are $(IC_1, IC_2, IC_3) = (0.01, 0.01, 0.01)$.

The chaos encountered during the numerical simulations in Figures 2 (a) to (c) can be reproduced using electronic execution as shown in Figure 6.

CONTROL OF COEXISTING ATTRACTORS

Chaos and coexisting attractors encountered in PMSMLT are undesirable dynamical states in electrical machines. The linear augmentation control method is used to control the coexistence between chaos and no oscillations in PMSMLT (Sharma *et al.* 2015). The controlled system is written:

$$\frac{dx}{dt} = -x + yz, \tag{6a}$$

$$\frac{dy}{dt} = -y - xz + \gamma z, \tag{6b}$$

$$\frac{dz}{dt} = \sigma(y - z) + T_L, \tag{6c}$$

$$\frac{dv}{dt} = -\beta v - \delta(x - e), \tag{6d}$$

where Equation 6d is the control associated with the PMSMLT with β the decay parameter and δ the coupling parameter between the linear controller system and PMSMLT to be controlled. Figure 7 presents the superposition of the bifurcation diagrams obtained by control for the initial conditions having led to the coexistence between the chaos having the initial conditions $(x_0, y_0, z_0) = (0, 0, 0)$ and the fixed point having the initial conditions $(x_0, y_0, z_0) = (0, 0.2, 0)$.

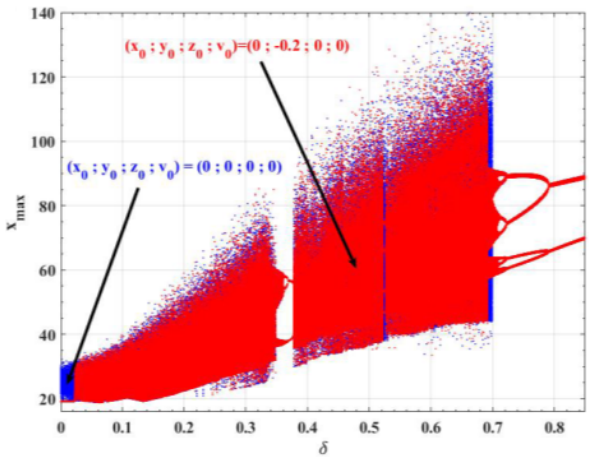

Figure 7 Bifurcation diagrams of x as a function of the coupling parameter δ of the controlled system obtained for the two initial conditions leading to multistability: $(x_0, y_0, z_0) = (0, 0, 0)$ for the color blue and $(x_0, y_0, z_0) = (0, 0.2, 0)$ for the color red. The parameter values are as follows: $\sigma = 5.46$, $\gamma = 20$, $T_L = 6.5$, $\beta = 0.01$, and $e = 5$.

In Figure 7, it reveals that when the coupling $\delta \leq 0.02$, the PMSMLT presents a coexistence of chaos and no oscillations. When this coupling force δ is adjusted in an increasing manner, the dynamics of the system tends towards monostability, corresponding to a limit cycle with two periods. Thus, Figure 7 shows the transition from multistability to monostability. In order to highlight the different transitions leading to the control of multistability in the PMSMLT, the phase portraits are made in Figure 8.

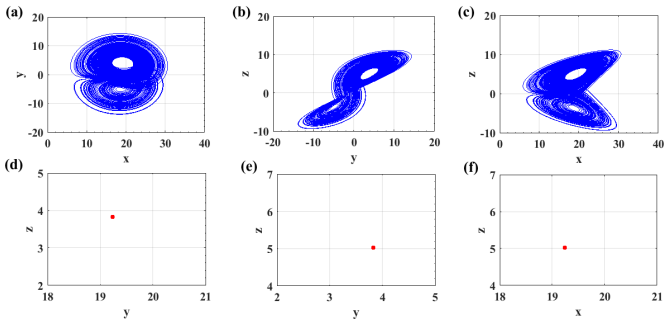

Figure 8 Phase portraits showing the coexistence of the fixed point and chaos obtained for $\sigma = 5.46$, $\gamma = 20$, $T_L = 6.5$, $\beta = 0.01$, $e = 5$, and $\delta = 0$. The lines in blue are obtained using the initial conditions $(x_0, y_0, z_0) = (0, 0, 0)$, while the lines in red are obtained using the initial conditions $(x_0, y_0, z_0) = (0, 0.2, 0)$.

For $\delta = 0$, the starting coexistence between chaos and no oscillations is illustrated in Figure 8. Figure 9 highlights the monostability of the PMSMLT by plotting the phase portraits.

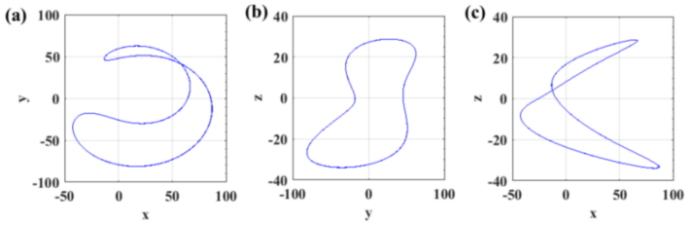

Figure 9 Phase portraits following the planes: (a) (x-y), (b) (y-z), and (c) (x-z) obtained for $\sigma = 5.46$, $\gamma = 20$, $T_L = 6.5$, $\beta = 0.01$, $e = 5$, and $\delta = 0.8$.

For $\delta = 0.8$, we observe monostability in the PMSMLT characterized by a two-period limit cycle illustrated by Figure 9.

CONCLUSION

The aim of this paper was to study the dynamics, electronic implementation, and control in permanent magnet synchronous motors with load torque (PMSMLT). PMSMLT presented no oscillations, periodic oscillations, chaos, and the coexistence between no oscillations and chaos, this for certain values of the load torque. The electronic implementation of the PMSMLT was carried out using the PSPICE software. The results obtained from the numerical simulations and the electronic implementation of the PMSMLT agree. The linear augmentation control method used made it possible to eliminate the coexistence between no oscillations and chaos in the PMSMLT. This paper helps in the field of electrical drives for industrial processes with variable speed and variable torque.

Availability of data and material

Not applicable.

Conflicts of interest

The authors declare that there is no conflict of interest regarding the publication of this paper.

Ethical standard

The authors have no relevant financial or non-financial interests to disclose.

LITERATURE CITED

Borisavljevic, A., 2013 *Limits, Modeling and Design of High-Speed Permanent Magnet Machines*. Springer.

Chapman, S. J., 2005 *Electric Machinery Fundamentals*. McGraw-Hill series in electrical and computer engineering, McGraw-Hill.

Chau, K. and Z. Wang, 2011 *Chaos in Electric Drive Systems: Analysis, Control and Application*. John Wiley and Sons.

Cheukem, A., A. S. Kemnang Tsafack, S. Takougang Kingni, C. C. André, and J. R. Mboupda Pone, 2020 Permanent magnet synchronous motor: chaos control using single controller, synchronization and circuit implementation. SN Applied Sciences **2**: 1–11.

Dong-lian, Q., J.-J. Wang, and Z. Guang-zhou, 2005 Passive control of Permanent Magnet Synchronous Motor chaotic systems. Journal of Zhejiang University SCIENCE **6**: 728–732.

Du-Qu, W. and Z. Bo, 2009 Controlling chaos in permanent magnet synchronous motor based on finite-time stability theory. Chinese Physics B **18**: 1399.

El-Sharkawi, M. A., 2000 *Fundamentals of Electric Drives*. Electrical Engineering Series, Brooks/Cole.

Fitzgerald, A. E., C. Kingsley, and S. Umans, 1991 *Electric Machinery*. Electrical Engineering Series, McGraw-Hill Companies,Incorporated.

Hua, C., Y. Wang, L. Zhang, and W. Ding, 2022 Stability and stabilization for the coupling permanent magnet synchronous motors system with input delay. Nonlinear Dynamics **107**: 3461–3471.

Hughes, A., 2006 *Electric Motors and Drives: Fundamentals, Types and Applications*. Electrical Engineering, Elsevier/Newnes.

Iqbal, A. and G. K. Singh, 2019 Chaos control of permanent magnet synchronous motor using simple controllers. Transactions of the Institute of Measurement and Control **41**: 2352–2364.

Leine, R. and H. Nijmeijer, 2004 *Dynamics and bifurcations of non-smooth mechanical systems*. Lecture notes in applied and computational mechanics, Springer, Germany.

Luo, S., 2014 Adaptive fuzzy dynamic surface control for the chaotic permanent magnet synchronous motor using Nussbaum gain. Chaos: An Interdisciplinary Journal of Nonlinear Science **24**: 33135.

Luo, S., J. Wang, Z. Shi, and Q. Qiu, 2014 Output Feedback Adaptive Dynamic Surface Control of Permanent Magnet Synchronous Motor with Uncertain Time Delays via RBFNN. Discrete Dynamics in Nature and Society **2014**: 315634.

Machowski, J., J. W. Bialek, and J. R. Bumby, 2012 Power System Dynamics. Stability and Control. John Wiley and Sons .

Maeng, G. and H. H. Choi, 2013 Adaptive sliding mode control of a chaotic nonsmooth-air-gap permanent magnet synchronous motor with uncertainties. Nonlinear Dynamics **74**: 571–580.

Mao, W.-L. and G.-Y. Liu, 2019 Development of an Adaptive Fuzzy Sliding Mode Trajectory Control Strategy for Two-axis PMSM-Driven Stage Application. International Journal of Fuzzy Systems **21**: 793–808.

Santoso, S. and H. W. Beaty, editors, 2018 *Standard Handbook for Electrical Engineers*. McGraw-Hill Education, New York, 17th edition.

Say, M. G. and E. O. Taylor, 1980 Direct current machines. (No Title) .

Sharma, P. R., M. D. Shrimali, A. Prasad, N. V. Kuznetsov, and G. A. Leonov, 2015 Control of multistability in hidden attractors. The European Physical Journal Special Topics **224**: 1485–1491.

Vadivel, R., Z. T. Njitacke, L. Shanmugam, P. Hammachukiattikul, and N. Gunasekaran, 2023 Dynamical analysis and reachable set estimation of t-s fuzzy system with permanent magnet syn-

chronous motor. Communications in Nonlinear Science and Numerical Simulation **125**: 107407.
Wildi, T., 2006 *Electrical Machines, Drives, and Power Systems*. Pearson Prentice Hall, fifth edition.
Yamdjeu, G., B. Sriram, S. T. Kingni, K. Rajagopal, and A. Mohamadou, 2024 Analysis, microcontroller implementation and chaos control of non-smooth air-gap permanent magnet synchronous motor. Pramana - Journal of Physics **98**: 126.

How to cite this article: Fotsa, R. T., Papemsi, P. K., Kuete, G. P. A., Pone, J. R. M., Naoussi, S. R. D., Momo, F., and Ele, P. Permanent Magnet Synchronous Motor with Load Torque: Dynamics, Circuitry Execution and Control. *Chaos and Fractals*, 2(1), 14-19, 2025.

ADBA Chaos and Fractals
Cutting-Edge Scientific Solutions

e-ISSN: 3023-8951
RESEARCH ARTICLE
Vol.2 / No.1 / 2025 / pp.20-27
https://doi.org/10.69882/adba.chf.2025014

Investigation of the Impact of Alloying Elements on the Mechanical Properties of Superalloys Using Explainable Artificial Intelligence

Berkay Emin [*,1], **Yusuf Uzunoğlu** [α,2] **and Yusuf Alaca** [β,3]

[*]Electronics and Automation, Osmancik Omer Derindere Vocational College, Hitit University, Çorum, Türkiye, [α]Materials Science and Engineering, Erciyes University, 38039 Kayseri, Türkiye, [β]Computer Engineering, Hitit University, 19030 Çorum, Türkiye.

ABSTRACT This study investigates the impact of alloying elements on the mechanical properties of Ni-Cr-Fe-based superalloys using a computational materials science approach. Fifty different compositions of superalloys, commonly known as Inconel and Incoloy, were modeled using the JMatPro software. The mechanical properties, including 0.2% proof stress (MPa), fracture stress (MPa), and Young's modulus (GPa), were simulated across a temperature range from 540 °C to 920 °C at 20 °C intervals for each alloy. The simulation generated a comprehensive dataset comprising 1000 rows. This dataset was then utilized to train an explainable artificial intelligence (XAI) model, leveraging advanced techniques such as SHAP (SHapley Additive exPlanations), LIME (Local Interpretable Model-agnostic Explanations), and Partial Dependence Plots (PDP). The dataset was analyzed using an XAI-based regression model employing the XGBoost algorithm. The interpretability graphs were analyzed to evaluate the individual contributions of each alloying element to the mechanical properties over the entire temperature range. The findings provide detailed insights into the positive or negative effects of alloying elements, enabling a better understanding of their role in optimizing superalloy performance under various thermal conditions. This work highlights the potential of integrating computational materials modeling and explainable AI to advance the design and development of high-performance materials.

KEYWORDS
Explainable artificial intelligence
Computational materials
Superalloys
mechanical properties

INTRODUCTION

Nickel-based superalloys have long been integral to industries requiring materials that sustain mechanical strength and resistance to oxidation at high temperatures, such as aerospace, power generation, and petrochemical applications (Hamdi and Abedi 2024). These alloys derive their exceptional properties from complex microstructures, primarily composed of austenitic γ-matrix and strengthening γ' or γ'' phases (Zhang *et al.* 2023). Elements like chromium, molybdenum, and aluminum are strategically added to enhance specific attributes, including oxidation resistance, creep strength, and precipitation hardening. However, the intricate interplay of these alloying elements under varying operational conditions remains a subject of extensive investigation (Monzamodeth *et al.* 2021).

Recent advancements in computational tools, such as JMatPro, have enabled high-throughput simulations of phase equilibria, mechanical properties, and thermal stability across a range of compositions and temperatures (Zhu *et al.* 2024). These simulations provide foundational insights for alloy design but often fail to elucidate the nuanced contributions of individual elements. Consequently, machine learning and explainable AI (XAI) approaches, such as SHAP (SHapley Additive exPlanations) and LIME (Local Interpretable Model-agnostic Explanations), have gained traction for interpreting the role of compositional variables in material properties (Zhang *et al.* 2024). These methods have proven effective in correlating microstructural features with performance metrics, such as proof stress and fracture toughness, particularly in alloys subjected to high-temperature deformation (Huang *et al.* 2024).

Manuscript received: 16 December 2024,
Revised: 15 January 2025,
Accepted: 21 January 2025.

[1]berkayemin@hitit.edu.tr (**Corresponding author**).
[2]4012640009@erciyes.edu.tr
[3]yusufalaca@hitit.edu.tr

The Ni-Cr-Fe alloy system, including widely used grades such as Inconel and Incoloy, exemplifies the importance of compositional control. Studies have shown that chromium improves oxidation resistance, while iron balances cost-effectiveness and thermal stability (Cheng *et al.* 2024). However, the presence of secondary phases, such as topologically close-packed (TCP) structures, can detrimentally impact mechanical properties, necessitating careful optimization of alloying elements and processing conditions (Zhang *et al.* 2023).

This study builds on the existing body of knowledge by integrating computational materials science and XAI methodologies to analyze the mechanical properties of Ni-Cr-Fe superalloys. By leveraging a dataset comprising simulations at incremental temperatures, it aims to quantify the contributions of each alloying element to properties like proof stress, fracture stress, and Young's modulus. The findings are expected to provide actionable insights for alloy design and performance optimization in high-temperature applications.

MATERIALS AND METHODS

This study employs a computational materials science approach combined with explainable artificial intelligence (XAI) to investigate the influence of alloying elements on the mechanical properties of Ni-Cr-Fe-based superalloys. Using JMatPro software, fifty different Ni-Cr-Fe alloy compositions, including Inconel and Incoloy, were modeled to simulate mechanical properties such as 0.2% Proof Stress (MPa), Fracture Stress (MPa), and Young's Modulus (GPa) over a temperature range of 540°C to 920°C at 20°C intervals. The simulations produced a dataset comprising 1000 entries, which served as input for an XAI-driven regression model utilizing the XGBoost algorithm. This model enabled the generation of SHAP (SHapley Additive exPlanations), LIME (Local Interpretable Model-agnostic Explanations), and PDP (Partial Dependence Plots) to elucidate the contribution of individual alloying elements to the mechanical properties across the temperature range.

Figure 1 illustrates the proposed model workflow, detailing the integration of computational simulations, dataset generation, machine learning model training, and XAI-based interpretative analysis. This framework aims to provide comprehensive insights into how each alloying element influences mechanical performance, paving the way for optimized superalloy design tailored to high-temperature applications.

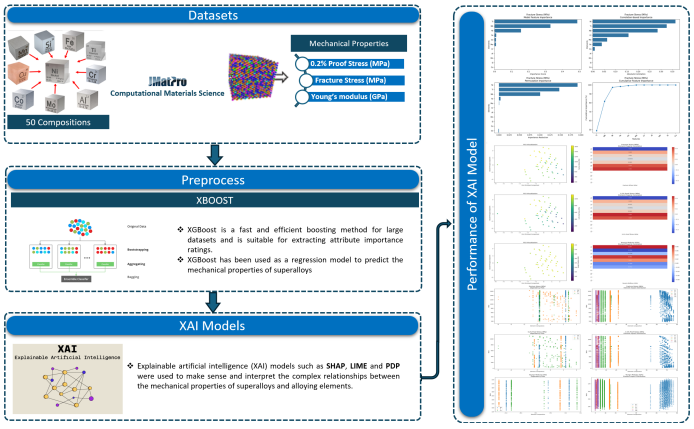

Figure 1 Proposed Model

Dataset Preparation

This study focuses on Ni-Cr-Fe-based superalloys, such as Inconel and Incoloy, widely used in industry due to their high mechanical performance and ability to undergo precipitation hardening through solution treatment and aging processes. These heat treatment procedures stabilize the microstructure and enhance the material's ability to maintain mechanical properties at elevated temperatures over prolonged periods. Precipitation hardening is a key process that significantly improves the strength of Inconel and Incoloy alloys at high temperatures (Zhang 2019).

The compositions modeled in JMatPro were based on key elements of Ni-Cr-Fe superalloys, including Ni, Cr, Fe, Co, Mo, Nb, and Ti. Elements such as Al, Mn, Si, and Cu, which enable precipitation hardening and aging treatments, were held constant at specific levels across all alloy combinations (ASM International 1991). The alloy compositions were designed to optimize their mechanical properties by simulating the solution treatment and aging parameters. The weight fractions of the primary elements were varied within the following ranges: 50–75% Ni, 14–21% Cr, 5–15% Fe, 0–2% Co, 0–3% Mo, 1–5% Nb, and 1–2.5% Ti. Additionally, the following weight fractions were kept constant in all compositions: 0.5% Al, 1% Mn, 0.5% Si, and 0.5% Cu. Phase Fraction Diagrams and TTT (Time-Temperature-Transformation) Diagrams were generated for each alloy composition. Table 1 outlines the range of alloying elements used to design 50 distinct alloy compositions. Each composition was evaluated across 20 different temperatures ranging from 540°C to 920°C, in increments of 20°C. The simulated mechanical properties - 0.2% Proof Stress (MPa), Fracture Stress (MPa), and Young's Modulus (GPa) - were recorded for each temperature. As a result, a comprehensive dataset consisting of 50 alloy compositions and their mechanical properties across 20 temperature points was developed, yielding a total of 1,000 data rows.

Table 1 Elemental Composition Ranges of Alloys in the Dataset (values represent wt%)

Ni (%)	Cr (%)	Fe (%)	Co (%)	Mo (%)	Nb (%)	Ti (%)	Al (%)	Mn (%)	Si (%)	Cu (%)
50–75	14–21	5–15	0 and 2	0 and 3	1 and 5	1 and 2.5	0.5	1	0.5	0.5

Table 2 illustrates an example of the dataset, showcasing two alloy compositions. The second alloy composition differs from the first by the addition of 1% Co, which is observed to enhance the mechanical property values. This dataset serves as the foundation for subsequent analysis, enabling the systematic investigation of how individual alloying elements influence the mechanical behavior of superalloys under various thermal conditions.

Heat Treatment Simulation and Microstructure Optimization The simulations for this study were performed using the JMatPro software, which is based on principles of computational materials science. The software was used to model 50 different compositions of Ni-based superalloys, with specific alloying elements added to nickel at varying proportions. For each composition, Phase Fraction Diagrams and TTT (Time-Temperature-Transformation) Diagrams were generated and analyzed to determine the optimal heat treatment temperature for forming the two precipitate phases, gamma prime (γ') and gamma double prime (γ''). These phases were selected as they contribute significantly to the mechanical

Table 2 The First Two Compositions (C1, C2) in the Dataset

Ni (%)	Cr (%)	Fe (%)	Co (%)	Mo (%)	Nb (%)	Ti (%)	Al (%)	Mn (%)	Si (%)	Cu (%)	Temperature (ºC)	0.2% Proof Stress (MPa)	Fracture Stress (MPa)	Young's Modulus (GPa)
67	22	5	0	0	1	2.5	0.5	1	0.5	0.5	920.0	89.27	332.99	137.5
67	22	5	0	0	1	2.5	0.5	1	0.5	0.5	900.0	165.08	551.78	139.74
67	22	5	0	0	1	2.5	0.5	1	0.5	0.5	880.0	218.35	729.71	141.92
⋮	⋮	⋮	⋮	⋮	⋮	⋮	⋮	⋮	⋮	⋮	⋮	⋮	⋮	⋮
67	22	5	0	0	1	2.5	0.5	1	0.5	0.5	580.0	768.34	1380.38	168.64
67	22	5	0	0	1	2.5	0.5	1	0.5	0.5	560.0	767.79	1392.7	170.14
67	22	5	0	0	1	2.5	0.5	1	0.5	0.5	540.0	767.28	1404.43	171.62
66	22	5	1	0	1	2.5	0.5	1	0.5	0.5	920.0	110.51	387.26	138.29
66	22	5	1	0	1	2.5	0.5	1	0.5	0.5	900.0	176.07	582.59	140.53
66	22	5	1	0	1	2.5	0.5	1	0.5	0.5	880.0	226.97	756.4	142.73
⋮	⋮	⋮	⋮	⋮	⋮	⋮	⋮	⋮	⋮	⋮	⋮	⋮	⋮	⋮
66	22	5	1	0	1	2.5	0.5	1	0.5	0.5	580.0	770.05	1382.07	169.35
66	22	5	1	0	1	2.5	0.5	1	0.5	0.5	560.0	769.51	1394.4	170.85
66	22	5	1	0	1	2.5	0.5	1	0.5	0.5	540.0	769.02	1406.14	172.34

properties of the alloys (Peachey *et al.* 2024). The resulting mechanical property values at the determined temperatures were incorporated into the dataset.

Each composition was simulated using heat treatment parameters tailored to produce gamma (γ), gamma prime (γ'), and gamma double prime (γ'') phases while excluding undesired phases such as delta, eta, laves, MC, M6C, and M3B2. These phases were disregarded due to their formation only during prolonged aging processes and their potential to negatively affect mechanical properties (Schulz *et al.* 2024). The simulations were performed under equilibrium conditions, ensuring that unwanted phases, which would typically appear under extremely slow cooling or extended durations in real-world applications, were excluded. This approach enabled the modeling of results that accurately reflect practical heat treatment processes. The grain size of the matrix phase (gamma)

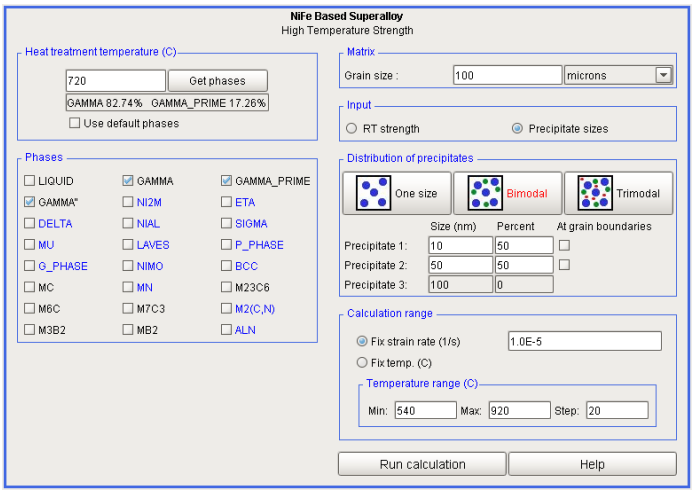

Figure 2 Input Parameters and Bimodal Distribution Settings for Ni-Based Superalloy Simulation in JMatPro

was set at 100 microns, while the precipitate sizes for gamma prime (γ') and gamma double prime (γ'') phases were defined as 10 nm and 50 nm, respectively. To simulate the microstructure effectively, the "Bimodal" distribution option was selected, as shown in Figure 2. The heat treatment parameters, including temperature and duration, were optimized for each composition to ensure the complete precipitation of gamma prime (γ') and gamma double prime (γ'') phases within the matrix (Gontcharov and Lowden 2024). The temperature range for these simulations was set between 540°C and 920°C, ensuring a comprehensive evaluation of the material's mechanical properties across relevant service conditions.

The results from these simulations provided critical insights into the microstructure and mechanical properties of the modeled alloys, serving as the foundation for further analysis and optimization.

Development of the Explainable Artificial Intelligence Model In this study, a powerful machine learning algorithm, the XGBoost regression model, is used and Explainable Artificial Intelligence (XAI) methods are integrated to ensure the explainability of the artificial intelligence model developed for the prediction of mechanical properties of Ni-Cr-Fe based superalloys.

XGBoost (Extreme Gradient Boosting) is a high-performance and scalable gradient boosting algorithm widely used in machine learning. Developed by Chen and Guestrin (2016), this method is particularly notable for its capacity to achieve effective results on large datasets and high-dimensional feature spaces. XGBoost is a decision tree-based model that gradually adds new trees at each iteration to reduce errors. This process aims to minimize overfitting while increasing the generalization capability of the model. Furthermore, XGBoost's regularization techniques keep the model's complexity under control, resulting in more robust and reliable predictions. Thanks to its parallel processing capabilities and optimized computational processes, XGBoost outperforms other gradient boosting algorithms in terms of both speed and accuracy. Thanks to these features, XGBoost has a wide range of applications in both academic research and industrial applications (Chen and Guestrin 2016).

To make the inner workings and decision-making processes of the model transparent, widely accepted XAI methods such as SHAP (SHapley Additive exPlanations), LIME (Local Interpretable Model-Agnostic Explanations) and Partial Dependence Plots (PDP) were used.

SHAP is an advanced explainable artificial intelligence (XAI) method developed to interpret the predictions of machine learning models transparently and understandably. Using Shapley values based on game theory, SHAP distributes the contribution of each feature to model prediction fairly and consistently. This approach reveals the inner workings of complex and black box models, making the reasons for model decisions more understandable for users. SHAP, as defined by Lundberg and Lee (2017), can provide both local (for individual forecasts) and global (model-wide) explanations. One of the key advantages of SHAP is that it is compatible with different types of models and can work model independently, making it ideal for a wide range of applications. Furthermore, the descriptions obtained with SHAP provide reliability and transparency for model users, which increases model acceptance, especially in high-risk areas (Lundberg and Lee 2017).

LIME is an explainable artificial intelligence (XAI) method developed to make the predictions of complex machine learning models locally understandable and interpretable. This method, described by Ribeiro, Singh, and Guestrin (2016), creates a simple and local model to explain a particular prediction of any model. LIME generates new data around a specific data point decided by the target model and trains a simple model (e.g., linear regression) on this data, trying to understand the behavior of the original model on this data point. In this way, it provides a visual and quantitative representation of how complex and black box models are affected by which inputs for certain predictions. LIME's model-agnostic nature makes it compatible with different machine learning algorithms and offers a wide range of applications. These features make LIME a valuable tool for engineering-oriented problems such as the optimization of mechanical properties of superalloys Ribeiro *et al.* (2016).

Partial Dependence Plots (PDPs) are an analysis method used in machine learning models to visualize the effect of one or more features on the model output. PDPs show, on average, how the model's predictions change if the value of the examined feature changes while all other features are held constant. This method is particularly important for understanding the general trends of complex and so-called black box models and for interpreting the effects of specific features on the model. The PDPs developed by Friedman (2001) allow us to better understand the effects of features on target variables such as mechanical properties by revealing how the model reacts to which features. This makes it possible to determine which elements and ranges are critical in optimizing the mechanical properties of superalloys (Friedman 2001).

RESULTS AND DISCUSSION

In this chapter, a comprehensive analysis of the effect of alloying elements on the mechanical properties of Ni-Cr-Fe based superalloys is presented by using descriptive artificial intelligence (XAI) methods. The study modeled the mechanical properties (tensile strength, proof stress, and modulus of elasticity) at temperatures between 540°C and 920°C for 50 different compositions and analyzed these data with XAI methods to highlight the effects of alloying elements.

In the study, data generated with JMatPro software were analyzed with an XAI-based regression model shaped using the XGBoost algorithm. The findings revealed the significant effects of elements such as Titanium (Ti), Niobium (Nb), and Nickel (Ni) on tensile strength and proof stress, while emphasizing the importance of Cobalt (Co) and Molybdenum (Mo) for the modulus of elasticity. The visibility obtained from the XAI analyses details numerically and graphically the positive and negative effects of each element on the mechanical properties, and a meaningful roadmap for alloy design is presented below. Figure 3 presents the results

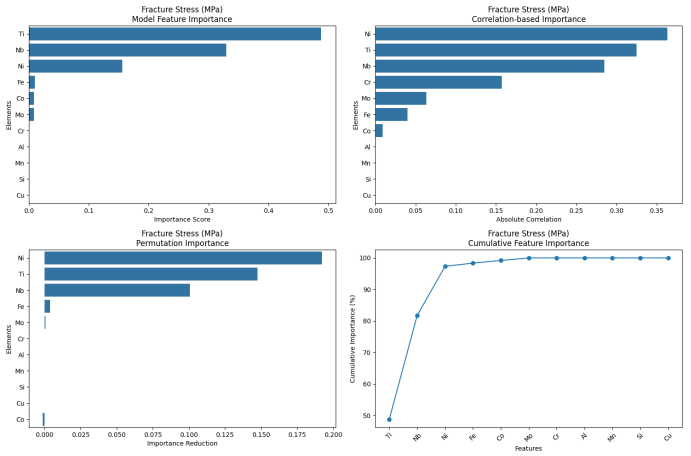

Figure 3 Importance of Alloying Elements on Fracture Stress (MPa)

of different analysis methods to explain the influence of alloying elements on Fracture Stress. The model feature importance plot shows the feature importance scores determined by the artificial intelligence model. In this analysis, Titanium (Ti) stands out as the element with the highest influence, while Niobium (Nb) and Nickel (Ni) rank second and third, respectively. Other elements such as Fe (Iron), Mo (Molybdenum), and Cr (Chromium) have lower levels of significance. This suggests that the effects on fracture strength are largely associated with Ti, Nb, and Ni.

The correlation-based importance graph evaluates the linear relationship between the fracture stress and each element based on absolute correlation values. According to this method, Nickel (Ni) has the highest correlation coefficient and shows a strong influence on fracture strength. Titanium (Ti) and Niobium (Nb) also exhibit high correlation values on fracture strength, while elements such as Cr and Mo have a lower effect. This analysis provides an important perspective to quantify the magnitude of direct and indirect effects on fracture strength.

Permutation importance plot is another analysis method that evaluates the contribution of each element to model performance. According to this method, Nickel (Ni) was identified as the most important element for model performance, followed by Titanium (Ti) and Niobium (Nb). The contributions of Fe, Mo, and Cr are relatively low. These results indicate that Ni, Ti, and Nb are the elements that improve the fracture stress prediction performance of the model the most.

Finally, the cumulative feature importance graph describes the cumulative impact of the features on the model. As can be seen in the graph, the combined contributions of Titanium (Ti), Niobium (Nb), Nickel (Ni), and Iron (Fe) together explain more than 90% of the model performance. The total contribution of the other elements is very limited. This indicates that the content ratios of these four elements should be optimized properly in the design of high-performance superalloys. Figure 4 contains the results evaluating the effects of alloying elements on 0.2% Proof Stress by different analysis methods.

The model feature importance plot shows the feature importance scores calculated by the artificial intelligence model. This analysis reveals that Titanium (Ti) and Niobium (Nb) have the highest impact on proof stress. After these two elements, Nickel

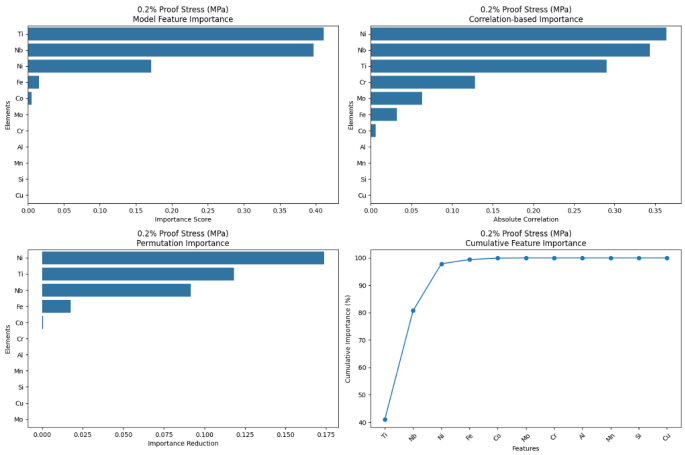

Figure 4 Importance of Alloying Elements 0.2% Proof Stress (MPa)

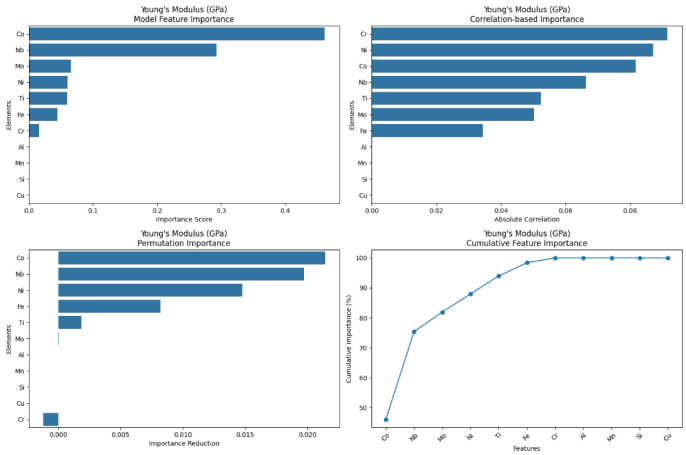

Figure 5 Importance of Alloying Elements on Young's Modulus (GPa)

(Ni) and Iron (Fe) contribute with lower importance levels. The effect of other elements (Co, Cr, Mo, Al, etc.) on model performance is very limited. These results emphasize that Ti and Nb are critical for 0.2% proof stress.

The correlation-based importance plot evaluates the linear relationship of each element with proof stress based on correlation. Here, Nickel (Ni) stands out as the element with the highest correlation coefficient. Niobium (Nb) and Titanium (Ti) rank second and third respectively, while other elements such as Cr and Mo show moderate correlation. This graph reveals that Ni has a significant influence on proof stress and that the contributions of Nb and Ti are also significant.

The permutation importance plot evaluates the contribution of the properties to the model performance in a commutativity-based approach. In this method, Nickel (Ni) is identified as the element with the highest impact on proof stress. Ti and Nb are ranked second and third in this order, with other elements such as Fe contributing less. Permutation-based analysis shows that Ni, Ti, and Nb play a key role in explaining model performance.

Finally, the cumulative feature importance plot shows how much the alloying elements explain the model performance in total. This graph shows that Titanium (Ti), Niobium (Nb), Nickel (Ni), and Iron (Fe) can explain more than 90% of the total model performance. The cumulative contribution of the other elements is very low. This suggests that the content ratios of these four elements should be prioritized to optimize the 0.2% proof stress.

Figure 5 presents the findings of various analytical methods that examine the effects of alloying elements on Young's Modulus determination. The model features an importance plot that reveals the importance ranking of the elements that contribute to the predictive power of the model. The results show that Cobalt (Co) in particular has a strong influence on Young's Modulus, followed by Niobium (Nb), Molybdenum (Mo), and Nickel (Ni). This kind of significance analysis makes it clear which elements need to be considered more to improve the mechanical properties.

Another method of analysis, the correlation-based importance plot, investigates whether each element has a linear relationship with Young's Modulus. This approach shows that Chromium (Cr) has the highest linear relationship, with elements such as Nickel (Ni) and Cobalt (Co) making significant contributions to this relationship. However, it should be noted that in this method, the influence of elements on mechanical properties may not be limited to correlation alone. This suggests that Cr may have a more significant effect than expected under some conditions.

The permutation importance plot evaluates the weight of elements in model performance from a different perspective. Here, Cobalt (Co) again emerges as the leading element, followed by Niobium (Nb) and Nickel (Ni). This type of analysis highlights the need to integrate these elements more intensively into the design process to improve Young's Modulus.

Finally, the cumulative feature importance plot provides an overall picture of how much the elements together explain the model performance. It can be seen that the contributions of Co, Nb, and Mo explain a large part of the model performance, while the other elements make only marginal contributions. This indicates the importance of optimizing the doping ratios in designs for enhancing mechanical properties. Figure 6 comprehensively

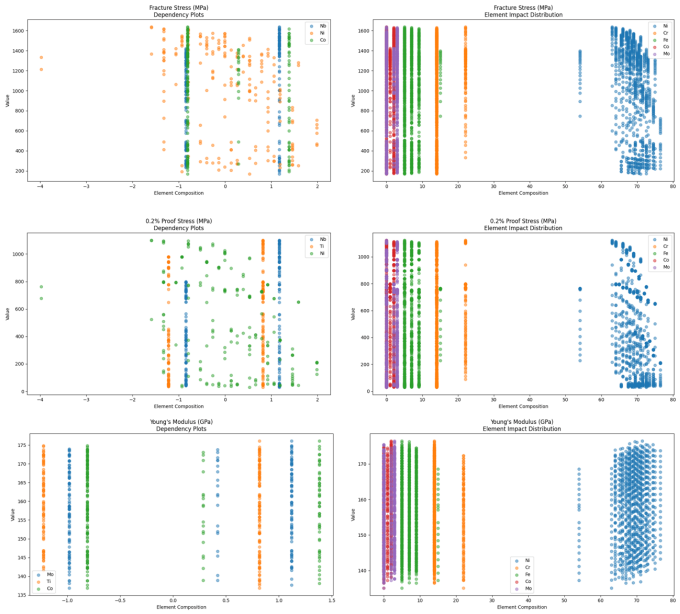

Figure 6 Dependence and Effect Distribution of Alloying Elements on Mechanical Properties

evaluates the effects of alloying elements on mechanical properties, both in terms of dependence and influence distribution. Firstly, the

analysis on Fracture Stress reveals that elements such as Niobium (Nb), Nickel (Ni), and Cobalt (Co) play a critical role in this mechanical property. In particular, a steady increase in fracture stress was observed with increasing Nb content. This trend emphasizes that Nb is a key element in terms of fracture strength. Similarly, Ni and Co also have significant effects on fracture stress, but these effects are concentrated in certain content ranges. The elemental influence distribution plots clearly show that the influence of Ni on the fracture stress is more dominant than that of the other elements and affects a wider range of contents.

Analysis of 0.2% Proof Stress shows that increasing the content of Nb and Ni significantly increases this property. These two elements are critical for optimizing proof stress. It was also observed that other elements such as Titanium (Ti) also have a positive contribution to proof stress, but the effect is not as dominant as Nb and Ni. The effect distribution plots emphasize the effects of Ni and Chromium (Cr) on this mechanical property, while Ni's strong influence on proof stress is once again confirmed. These analyses suggest that the Ni and Nb content ratios should be carefully controlled to improve the proof stress of superalloys.

Evaluations on Young's Modulus show that Molybdenum (Mo), Niobium (Nb), and Titanium (Ti) have positive effects on this mechanical property. In particular, it is noteworthy that an increase in the content ratio of Mo leads to a steady and significant improvement in the modulus of elasticity. This effect of Mo suggests that it plays a key role in improving elasticity. Nb and Ti also made significant contributions to Young's Modulus at certain content ranges and improved the mechanical performance of the superalloys. The effect distribution plots present the effects of Co and Nb on elasticity in a broad perspective, emphasizing the importance of these elements. Figure 7 presents a combination of Principal Component Analysis (PCA) and heat maps evaluating the correlation of elements with mechanical properties in superalloys. The graphs address three key mechanical properties, namely Fracture Stress, 0.2% Proof Stress, and Young's Modulus. The PCA visualizations present how the data is distributed in high-dimensional space reduced to two principal component axes, while the heat maps show the linear correlation of each element with these mechanical properties.

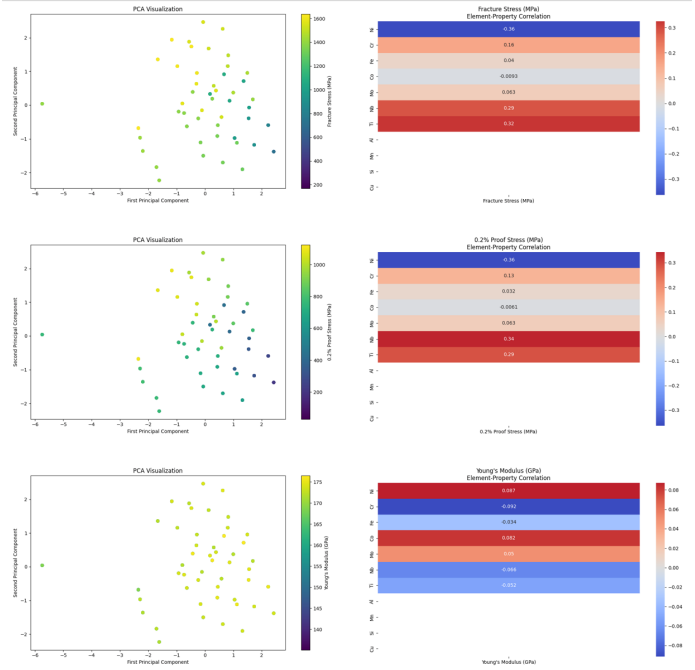

Figure 7 PCA Visualization and Element-Mechanical Property Correlations

The PCA visualization for Fracture Stress reveals that the data follow a specific distribution pattern and how this mechanical property can be correlated with different element compositions. The correlation heatmap shows that Niobium (Nb) has a negative correlation (-0.36), while Nickel (Ni) has a positive correlation (0.32). This indicates that Nb tends to decrease the fracture stress, while Ni has an increasing effect. The effects of Cobalt (Co) and other elements are relatively less pronounced.

The PCA analysis for 0.2% Proof Stress shows a similar distribution pattern, but the correlation map highlights the differences in the elements affecting this property. Nb again has a negative correlation (-0.36), whereas Ni (0.34) and Chromium (Cr, 0.29) stand out with positive correlations. This finding indicates that Nb has a decreasing effect on proof stress, while Ni and Cr improve this property.

The PCA visualization for Young's Modulus shows a more homogeneous distribution. The correlation map highlights that Molybdenum (Mo) has a significant positive effect (0.08) on the modulus of elasticity. In contrast, the effects of Nb and other elements on the modulus of elasticity are more limited. This confirms that Mo is one of the most critical elements for increasing elasticity.

According to the results given in Table 3, the developed model predicts the 0.2% Proof Stress and Fracture Stress properties of superalloys with reasonable accuracy (R^2 = 0.21 and 0.18). Low RMSE and MAE values indicate the reliability of the predictions. Although the performance of Young's Modulus could be improved, overall the model is considered a valuable tool in understanding the mechanical properties of superalloys. Figure 8 shows that the model has achieved significant success in understanding the relationships between mechanical properties and alloying elements. In particular, the results of the element complexity analysis revealed that Titanium (Ti) and Niobium (Nb) play a critical role in Fracture Stress and 0.2% Proof Stress, while Cobalt (Co) and Molybdenum (Mo) play a prominent role in Young's Modulus. This shows that

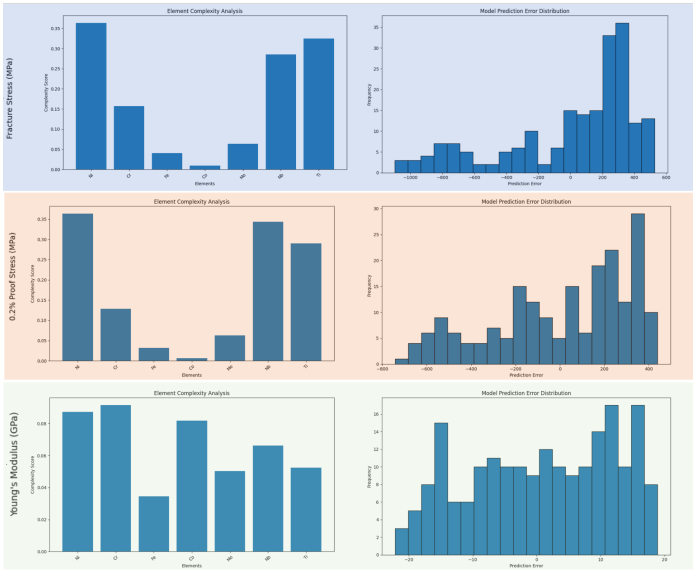

Figure 8 Element Complexity Analysis and Model Error Distribution

Table 3 Model Performance Metrics for Predicting Mechanical Properties

Property	Mean Squared Error	Root Mean Squared Error	R-squared	Mean Absolute Error	Mean Absolute Percentage Error	Cross-Validation R2 Mean	Cross-Validation R2 Std
0.2% Proof Stress (MPa)	95077.41	308.35	0.21	266.15	1.79	0.18	0.09
Fracture Stress (MPa)	171941.42	414.66	0.18	338.22	0.65	0.18	0.05
Young's Modulus (GPa)	125.25	11.19	-0.12	9.73	0.06	0.01	0.01

the model can accurately determine which elements make a greater contribution to optimizing mechanical properties. Moreover, when the distribution of prediction errors is analyzed, Young's Modulus predictions are within a narrow error range, indicating that the model works with high consistency for this property. The fact that the prediction errors for Fracture Stress and 0.2% Proof Stress are generally concentrated in a reasonable range also supports the overall accuracy of the model. These findings show that the model can provide reliable predictions for the design of superalloys in high-temperature applications and can be used as an effective tool for optimizing the effects of alloying elements. The results presented in Figure 9 show that the model can predict the Fracture Stress (MPa) and 0.2% Proof Stress (MPa) with significant accuracy. In particular, the relationship between predicted values and actual values for these two mechanical properties indicates that the model performs reliably in these areas. The positive trends observed in the R^2 distribution support the model's ability to consistently explain these properties and provide accurate predictions. This indicates that the model has effectively learned the interactions between alloying elements and mechanical properties. These results demonstrate that the model is a reliable tool for predicting critical mechanical properties such as Fracture Stress and 0.2% Proof Stress, which can provide useful insights in alloy design.

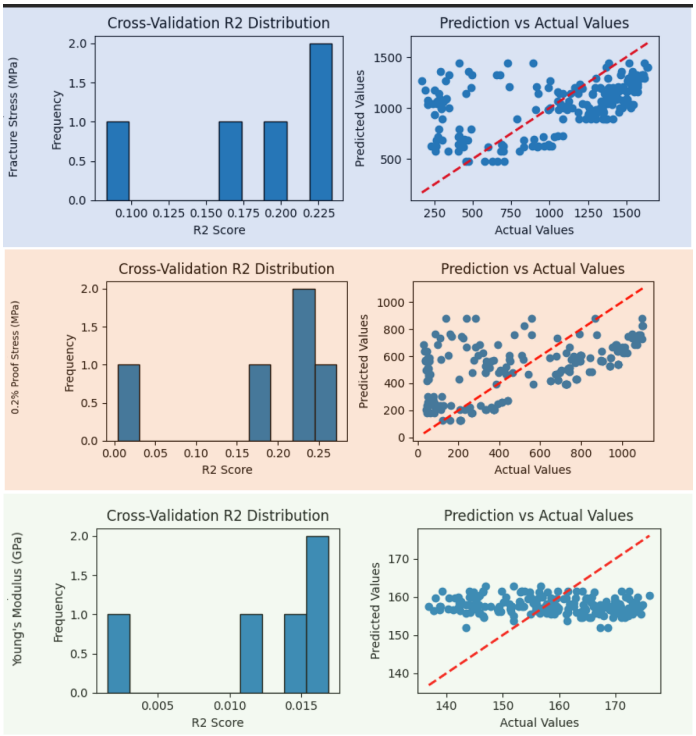

Figure 9 Cross Validation R^2 Distribution and Prediction vs Actual Value

CONCLUSION

This study comprehensively investigated the mechanical properties of Ni-Cr-Fe based superalloys under different alloying elements and temperature ranges through computational materials science approaches and explainable artificial intelligence (XAI) methods. The large data set obtained as a result of simulations performed between 540°C and 920°C in 20°C increments was analyzed with the XGBoost-based regression model and interpreted in depth using XAI techniques such as SHAP, LIME and PDP. These methods revealed that critical mechanical properties such as 0.2% proof stress, fracture stress and Young's modulus are strongly influenced by Nb, Ti, Ni, Co and Mo content.

The findings show that the effects of certain alloying elements on mechanical properties at different temperature conditions can vary both quantitatively and qualitatively. For example, elements such as Nb and Ni were found to play more prominent roles on fracture stress and proof stress with increasing temperature, while elements such as Mo and Co showed remarkable contributions in terms of Young's modulus at elevated temperatures. This shows that mechanical properties are not only dependent on chemical composition but also on thermal conditions, which necessitates the optimization of alloy designs to provide stabilized and durable performance at elevated temperatures.

The obtained data and analyses emphasize that elemental contents and operating temperatures should be strategically determined in the design of high-performance superalloys. In particular, the use of elements such as Nb, Ni, Ti, Co and Mo in the right proportions will provide superior performance in terms of fracture stress and proof stress at high temperatures, while keeping elastic properties under control. In this context, the present findings provide important guidance for future research and industrial applications.

Availability of data and material

Not applicable.

Conflicts of interest

The authors declare that there is no conflict of interest regarding the publication of this paper.

Ethical standard

The authors have no relevant financial or non-financial interests to disclose.

LITERATURE CITED

ASM International, 1991 Heat Treating of Aluminum and Its Alloys. In *ASM Handbook Volume 4 Heat Treating*, pp. 1861–1960, ASM International.

Chen, T. and C. Guestrin, 2016 XGBoost: A Scalable Tree Boosting System. Proceedings of the 22nd ACM SIGKDD International Conference on Knowledge Discovery and Data Mining .

Cheng, Y., X. Zhao, W. Xia, Q. Yue, Y. Gu, *et al.*, 2024 The overview of the formation mechanisms of topologically close-packed phases in Ni-based single crystal superalloys. Materials Design **237**: 112582.

Friedman, J. H., 2001 Greedy function approximation: a gradient boosting machine. Annals of statistics pp. 1189–1232.

Gontcharov, A. B. and P. Lowden, editors, 2024 *The Development of Weldable Nickel-Based Superalloys and Technologies for Repair and Additive Manufacturing of Turbine Engine Components*, volume Advances i of *Advances in Materials for Power Plants*.

Hamdi, H. and H. R. Abedi, 2024 Thermal stability of Ni-based superalloys fabricated through additive manufacturing: A review. Journal of Materials Research and Technology **30**: 4424–4476.

Huang, F., Y. Song, Y. Li, H. Li, G. Zhao, *et al.*, 2024 Microstructure evolution of high-temperature deformation behavior of nickel based alloys for advanced ultra-supercritical applications. Materials Chemistry and Physics **314**: 128862.

Lundberg, S. M. and S.-I. Lee, 2017 A Unified Approach to Interpreting Model Predictions. In *Neural Information Processing Systems*.

Monzamodeth, R. S., B. Campillo, and O. Flores, 2021 Hydrogen diffusion in Ni-Cr-Fe system. Materials Today: Proceedings **42**: 1170–1175.

Peachey, D., Y. He, P. Zhang, J. Clark, Z. Hussain, *et al.*, editors, 2024 *ABD-1000AM: a Highly Processible Superalloy for Additive Manufacturing, Computationally Designed for 1000°C Applications*, volume Advances i of *Advances in Materials for Power Plants*.

Ribeiro, M. T., S. Singh, and C. Guestrin, 2016 "Why Should I Trust You?": Explaining the Predictions of Any Classifier. In *Proceedings of the 22nd ACM SIGKDD International Conference on Knowledge Discovery and Data Mining*, KDD '16, pp. 1135–1144, New York, NY, USA, Association for Computing Machinery.

Schulz, F., K. Lindgren, J. Xu, and E. Hryha, 2024 Gamma prime formation in nickel-based superalloy IN738LC manufactured by laser powder bed fusion. Materials Today Communications **38**: 107905.

Zhang, J., Y. Liu, Y. Cheng, H. Wang, A. Sha, *et al.*, 2024 Modeling of creep in nickel-based superalloy based on microtwinning mechanism. International Journal of Plasticity .

Zhang, X., 2019 Heat treatment effects on Inconel alloys. Journal of Materials Engineering. .

Zhang, Z., Z. Zhang, Y. Zhao, J. Huang, S. Chen, *et al.*, 2023 Insights into the effect of γ- or γ-precipitated phase types on resistance against harmful atoms of heterogeneous interface in nickel-based superalloys. Journal of Materials Research and Technology **26**: 3933–3946.

Zhu, L., H. Pan, B. Wei, L. Xiao, J. Guo, *et al.*, 2024 Investigation of microstructural stability and tensile deformation behavior of a novel PM Ni-based superalloy during long-term thermal exposure. Materials Science and Engineering A-structural Materials Properties Microstructure and Processing .

How to cite this article: Emin, B., Uzunoğlu, Y., and Alaca, Y. Investigation of the Impact of Alloying Elements on the Mechanical Properties of Superalloys Using Explainable Artificial Intelligence. *Chaos and Fractals*, 2(1), 20-27, 2025.